

## The Step-Mountain Coordinate: Model Description and Performance for Cases of Alpine Lee Cyclogenesis and for a Case of an Appalachian Redevelopment

FEDOR MESINGER\*

*Geophysical Fluid Dynamics Program, Princeton University, Princeton, New Jersey*

ZAVIŠA I. JANJIĆ, SLOBODAN NIČKOVIĆ AND DUŠANKA GAVRILOV

*Department of Physics and Meteorology, University of Belgrade, Yugoslavia*

DENNIS G. DEAVEN

*National Meteorological Center, NWS, NOAA, Washington, DC*

(Manuscript received 13 April 1987, in final form 28 January 1988)

### ABSTRACT

The problem of the pressure gradient force error in the case of the terrain-following (sigma) coordinate does not appear to have a solution. The problem is *not* one of truncation error in the calculation of space derivatives involved. Thus, with temperature profiles resulting in large errors, an increase in vertical resolution may not reduce and is even likely to *increase* the error. Therefore, an approach abandoning the sigma system has been proposed. It involves the use of "step" mountains with coordinate surfaces prescribed to remain at fixed elevations at places where they touch (and define) or intersect the ground surface. Thus, the coordinate surfaces are quasi-horizontal, and the sigma system problem is not present. At the same time, the simplicity of the sigma system is maintained.

In this paper, design of the model ("silhouette" averaged) mountains, properties of the wall boundary condition, and the scheme for calculation of the potential to kinetic energy conversion are presented. For an advection scheme achieving a strict control of the nonlinear energy cascade on the semistaggered grid, it is demonstrated that a straightforward no-slip wall boundary condition maintains conservation properties of the scheme with no vertical walls, which are important from the point of view of the control of this energy cascade from large to small scales. However, with that simple boundary condition considered, momentum is not conserved. The scheme conserving energy in conversion between the potential and kinetic energy, given earlier for the one-dimensional case, is extended to two dimensions.

Results of real data experiments are described, testing the performance of the resulting "step-mountain" model. An attractive feature of a step-mountain ("eta") model is that it can easily be run as a sigma system model, the only difference being the definition of ground surface grid point values of the vertical coordinate. This permits a comparison of the sigma and the eta formulations. Two experiments of this kind have been made, with a model version including realistic steep mountains (steps at 290, 1112 and 2433 m). They have both revealed a substantial amount of noise resulting from the sigma, as compared to the eta, formulation. One of these experiments, especially with the step mountains, gave a rather successful simulation of the perhaps difficult "historic" Buzzi-Tibaldi case of Genoa lee cyclogenesis. A parallel experiment showed that, starting with the same initial data, one obtains no cyclogenesis without mountains. Still, the mountains experiment did simulate the accompanying midtropospheric cutoff, a phenomenon that apparently has not been reproduced in previous simulations of mountain-induced Genoa lee cyclogenesis.

For a North American limited area region, experimental step-mountain simulations were performed for a case of March 1984, involving development of a secondary storm southeast of the Appalachians. Neither the then operational U.S. National Meteorological Center's Limited Area Forecast Model (LFM) nor the recently introduced Nested Grid Model (NGM) were successful in simulating the redevelopment. On the other hand, the step-mountain model, with a space resolution set up to mimic that of NGM, successfully simulated the ridging that indicates the redevelopment.

---

\* On leave from the Department of Physics and Meteorology, University of Belgrade. Current address: National Meteorological Center/NOAA, Washington, DC 20233.

---

Corresponding author address: Fedor Mesinger, Visiting Scientist, National Meteorological Center/NOAA, W/NMC2, WWB, Room 204, Washington, DC 20233.

### 1. Introduction: The sigma system problem

After being proposed by Phillips (1957), the sigma system has quickly become widely used in atmospheric models (e.g., WMO-ICSU 1974). In its original form, or modified so as to still keep the main idea of the terrain-following lowest coordinate surface, it perhaps

seemed to offer the only way of avoiding uncomfortable problems with the lowest boundary condition.

A problem that has received attention rather early in the development of sigma system primitive equation models is that of the noncancellation of errors in the two terms of the pressure gradient force (Smagorinsky et al. 1967). Many ideas aimed at understanding the origin of and reducing the error have been put forth; see, for example, the review paper by Mesinger and Janjić (1985). In particular, it has been pointed out that currently used pressure gradient force schemes can be derived as a result of a three-step procedure consisting of (i) calculation of geopotential at terrain-following coordinate surfaces, (ii) linear extrapolation/interpolation to constant pressure surfaces, and (iii) evaluation of the pressure gradient force on the constant pressure surfaces. The importance of a "coherency," or "hydrostatic consistency," of the techniques corresponding to steps (i) and (ii) has been stressed by Rousseau and Pham (1971) and Janjić (1977). Otherwise, the slope of the sigma (or other terrain-following coordinate) surface is calculated using one difference formula, and the correction needed to arrive at the slope of the constant pressure surface is calculated using another. If the slope of the sigma surface is large, a large error should then come as no surprise.

However, as also pointed out by Janjić, even the hydrostatically consistent schemes do not guarantee that the error will always be small, since their hydrostatic consistency is lost for steep slopes of sigma surfaces and/or thin sigma layers. As a result, in situations in which substantial errors may be expected (e.g., sharp changes in lapse rate), an increase in vertical resolution, in spite of an associated increase in formal accuracy, should be expected to lead to an *increase* in the error (Mesinger 1982). Contrary to some published optimistic views (Nakamura 1978; Sundqvist 1979), these errors can be large even for carefully designed schemes: say, in terms of geostrophic wind, of the order of  $10 \text{ m s}^{-1}$  for realistic mountain slopes and grid distances of about 150 km (Mesinger 1982; Mesinger and Janjić 1985). While no direct evidence exists of the problems of this kind in real data simulations, for obvious reasons, even occasional occurrences of large errors should be avoided if possible.

From the point of view of this problem with steep slopes and/or thin sigma layers, probably the best sigma system technique is that of explicit vertical interpolation to the desired constant pressure surface, as recently proposed by Mahrer (1984). This, in fact, is the very first method suggested to handle the difficulty (Smagorinsky et al. 1967; Kurihara 1968; Miyakoda 1973), which has been used at the Geophysical Fluid Dynamics Laboratory ever since. Recently, the explicit interpolation method has been addressed also by Tomine and Abe (1982) and by Mihailović and Janjić (1986); in the latter paper a scheme conserving energy in conversion between the potential and kinetic energy is

presented. In addition to the inherent complexity of calculations, which can make vectorization difficult, the problem of this technique is that it cannot be applied near the ground, where extrapolation to obtain subterranean geopotentials is needed (Mesinger and Janjić 1985). The possibility of evaluating the pressure gradient force with reduced horizontal grid step only along the model constant pressure surface which is above the ground hardly seems attractive in view of the severe linear stability penalty that this might impose (Mahrer 1984).

It is possible that the noise generation due to the sigma system is having a systematic effect on nonlinear interactions and therefore on the spectral distribution of energy, which could be linked to the widespread eddy versus zonal kinetic energy problem of numerical models (Sadourny 1985).

With potential temperature used as the vertical coordinate, simulation of the resting atmosphere is possible, since the coordinate surfaces of the resting atmosphere are then horizontal irrespective of the slope of the ground surface. In addition, with the pressure gradient force being a potential vector, its difference formulation can hardly be chosen in a hydrostatically inconsistent way. However, the error problem due to the *slope* of coordinate surfaces, for an atmosphere in motion, still remains (Mesinger and Janjić 1985). Thus, hydrostatic consistency will again be lost for steep slopes of isentropic surfaces and/or thin isentropic layers.

The use of pressure or of the geometric height as the vertical coordinate does not offer advantages comparable to those of isentropic coordinates. The technical difficulties, on the other hand, remain about the same. Thus, one would not expect these choices to gain in popularity. Indeed, a major operational forecasting model that had the pressure vertical coordinate, that of the United Kingdom Meteorological Office, has recently been replaced by a model formulated in terms of the sigma coordinate (e.g., Cullen 1985).

In summary, we suggest that with ever-increasing horizontal and vertical resolution, accompanied by a desire to have more realistic model mountains, the steplike mountain representation is a natural replacement for the sigma system, which may have been well suited for the low resolution models of the sixties and seventies.

## 2. The step-mountain coordinate

Lee cyclogenesis is an atmospheric phenomenon that is clearly a result of the effect of mountains. Since the representation of mountains is a major feature of the differences among possible choices of vertical coordinates, the ability of a model to simulate lee cyclogenesis may offer guidance as to how successful a particular choice actually is.

A remarkably successful idealized simulation of the Genoa lee cyclogenesis was achieved in an early effort

of Egger (1972). He has used the sigma system for gentle terrain slopes and a blocking approach with vertical walls to represent steep mountains.

The pressure gradient force problem of the terrain-following coordinates as well as other additional inconveniences (e.g., Simmons and Burridge 1981) are all a consequence of the slope of coordinate surfaces. The Egger method achieved approximately horizontal coordinate surfaces, but has suffered from two imperfections. It was not able to properly accommodate the three-dimensional geometry of steep mountains, and it had steep mountains change their elevation as a function of time.

Recently, Mesinger (1984) has pointed out a way to achieve approximately horizontal coordinate surfaces using a coordinate free of these problems. It can be written as

$$\eta = \frac{p - p_T}{p_S - p_T} \eta_S \quad (2.1)$$

with

$$\eta_S = \frac{p_{rf}(z_S) - p_T}{p_{rf}(0) - p_T}. \quad (2.2)$$

Here  $p$  is pressure; the subscripts  $T$  and  $S$  stand for the top and the ground surface values of the model atmosphere, respectively;  $z$  is geometric height, and  $p_{rf}(z)$  is a suitably defined reference pressure as a function of  $z$ . Furthermore, the ground surface heights  $z_S$  are permitted to take only a discrete set of values, chosen so that mountains are constructed from the three-dimensional grid boxes in the model (e.g., Mesinger and Janjić 1985). If this is felt to be advantageous,  $p_{rf}(0)$  in (2.2) can be replaced by  $p_{rf}(z_b)$ , with  $z_b$  representing a base elevation defined so as to include gentle slopes of the surface topography.

A schematic picture of the representation of mountains using this "step-mountain" coordinate is shown in Fig. 1. In this figure,  $u$ ,  $T$  and  $p_S$  represent the  $u$ -velocity component, temperature, and surface pressure grid points, respectively. The circled  $u$  grid points would be the points with zero values of the velocity components normal to sides of the mountain shown in the figure.

Following Kasahara (1974) and Simmons and Burridge (1981), using the coordinate (2.1), the governing equations for frictionless and adiabatic motion can be written as follows (Mesinger 1984):

$$\frac{d\mathbf{v}}{dt} + f\mathbf{k} \times \mathbf{v} + \nabla\Phi + \frac{RT}{p} \nabla p = 0, \quad (2.3)$$

$$\frac{dT}{dt} - \frac{\kappa T \omega}{p} = 0, \quad (2.4)$$

$$\frac{\partial}{\partial \eta} \left( \frac{\partial p}{\partial t} \right) + \nabla \cdot \left( \mathbf{v} \frac{\partial p}{\partial \eta} \right) + \frac{\partial}{\partial \eta} \left( \dot{\eta} \frac{\partial p}{\partial \eta} \right) = 0, \quad (2.5)$$

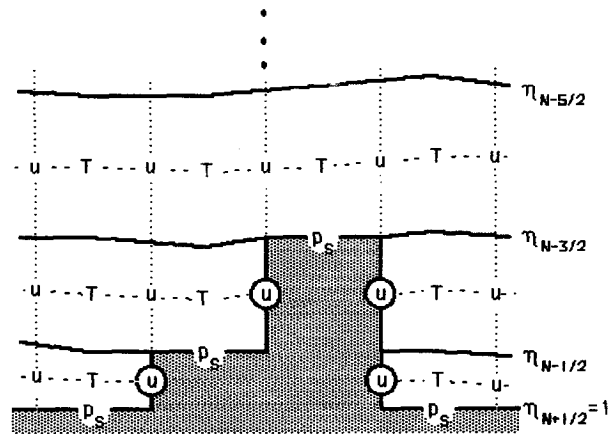


FIG. 1. A schematic picture of the representation of mountains using the coordinate (2.1)–(2.2).

$$\frac{\partial \Phi}{\partial \eta} = - \frac{RT}{p} \frac{\partial p}{\partial \eta}, \quad (2.6)$$

$$\omega \equiv \frac{dp}{dt} = - \int_0^{\eta_S} \nabla \cdot \left( \mathbf{v} \frac{\partial p}{\partial \eta} \right) d\eta + \mathbf{v} \cdot \nabla p, \quad (2.7)$$

$$\frac{\partial p_S}{\partial t} = - \int_0^{\eta_S} \nabla \cdot \left( \mathbf{v} \frac{\partial p}{\partial \eta} \right) d\eta, \quad (2.8)$$

$$\dot{\eta} \frac{\partial p}{\partial \eta} = - \frac{\partial p}{\partial t} - \int_0^{\eta_S} \nabla \cdot \left( \mathbf{v} \frac{\partial p}{\partial \eta} \right) d\eta. \quad (2.9)$$

Here  $d/dt$  is the material time derivative,  $\mathbf{v}$  is the horizontal velocity vector,  $f$  is the Coriolis parameter,  $\mathbf{k}$  is the vertical unit vector,  $\Phi$  is geopotential,  $R$  is the gas constant, and  $\kappa$  is  $R/c_p$ , where  $c_p$  is the specific heat at constant pressure. In arriving at (2.3) to (2.9), the boundary conditions assumed were  $p = \text{const}$  at the top boundary  $\eta = 0$ , and  $\dot{\eta} = 0$  at  $\eta = 0$  and at the horizontal parts of the ground surface  $\eta = \eta_S$ .

As seen in (2.3), the pressure gradient force in the "eta" system still consists of two terms; thus, one might be concerned as to what extent, if any, the pressure gradient as well as other sigma system problems will be alleviated with the eta coordinate. One should note that what matters in that respect is the slope of coordinate surfaces in terms of the differences in pressure; no problems arise in calculating, e.g., the pressure gradient force when the coordinate surfaces coincide with pressure surfaces. It is, therefore, of interest to consider the pressure difference between neighboring grid points. Denoting, as usual, by  $\Delta_x$  and  $\overline{(\quad)}^x$  the centered two-point differencing and averaging operator, respectively, applied along the direction of the  $x$ -axis, we obtain from (2.1),

$$\Delta_x p_\eta = \overline{\left( \frac{\eta}{\eta_S} \right)}^x \Delta_x p_S + \overline{(p_S - p_T)}^x \Delta_x \left( \frac{\eta}{\eta_S} \right). \quad (2.10)$$

With the sigma system,  $\eta_S$  is equal to unity, and  $\eta/\eta_S$

is constant in coordinate surfaces; thus, the second term on the right-hand side of (2.10) makes no contribution to  $\Delta_x p_\eta$ . In this situation, one would expect the largest values of  $\Delta_x p_\eta$  near the ground, where  $\eta/\eta_S$  is approaching unity. For extremely steep and realistic mountains, these maximum values could be of the order of several hundred millibars. With the step-mountain system, the second term on the right-hand side of (2.10) will then be different from zero and of the sign opposite to the first, and maximum values of  $\Delta_x p_\eta$  will be reduced. Cancellation will be complete when the atmosphere at the considered point is equal to the reference atmosphere. For a maximum departure from complete cancellation, say, at places such as just to the right of the highest plateau in Fig. 1, one can look for values of  $\Delta_x p_S$  as much above the reference values as possible, and at the same time those of  $\overline{p_S}^x$  as much below the reference values as possible. These are conflicting requirements; thus, it suffices to consider the contribution of the maximum possible departures of  $\Delta_x p_S$  only. Standard synoptic maps can be used for that purpose; in addition, the fact that with the eta system  $(\eta/\eta_S)^x$  is less than with the sigma system should be noted. In this way, one arrives at an estimate of the maximum values of  $\Delta_x p_\eta$  being at least an order of magnitude, and typically more than that, smaller than those of the sigma system.

An attractive feature of (2.1) is that, once a model code using (2.1) has been written, an option of having  $\eta_S = 1$  at all grid points can easily be included. Thus, *the same code can be run as a step-mountain and as a sigma system model*. This enables a comparison of the performance of the two systems, without the ever-present danger of having differences in results produced by a code error. Two experiments of this kind have been performed and will be discussed in one of the later sections.

For an extension of the step-mountain approach, as well as of some of the schemes considered earlier (Mesinger 1984), to two horizontal dimensions, several points need to be considered. The features intrinsically related to the definition of the vertical coordinate—choice of the horizontal grid, the hydrostatic equation and the vertical grid, the definition of mountains, and the definition and properties of the wall boundary condition—will be discussed in the following two sections. Along the way, a number of additional model details will be given, as set up for the experiments done to test the performance of the system. The experiments were made using two model regions, and some of these details will differ for the two regions used. One was a “European region,” the same as that used by Mesinger and Strickler (1982) for their simulations of Genoa lee cyclogenesis. The other was a “North American” region, with the choice of the region as well as of the horizontal resolution made so as to mimic the computational effort of the U.S. National Meteorological Center’s (NMC) so-called Nested Grid Model (NGM,

e.g., Hoke et al. 1985). Following these two sections, results of the experiments will be presented and discussed. Subsequently, a summary of main conclusions will be given. Finally, as an appendix, the derivation of the scheme used to conserve energy in transformations between kinetic and potential energy will be presented.

### 3. Horizontal grid, hydrostatic equation and the vertical grid, and definition of mountains

#### a. Horizontal grid

It has been clear ever since the pioneering work of Winninghoff (1968) and Arakawa (1970; also Arakawa and Lamb 1977) that various horizontal grids are not offering the same advantages for the simulation of large- and synoptic-scale atmospheric motions. Additional arguments have been summarized by Mesinger (1981) and by Janjić and Mesinger (1984). On balance, and with presently available finite-difference schemes, it would appear that there are overwhelming reasons against the use of the nonstaggered (*A*) grid as well as the staggered *D* grid.

The two remaining square grid possibilities are the staggered *C* grid and the semistaggered *B/E* grid; for some time now several of us have been using the semistaggered (*E*) grid (Mesinger 1973; Janjić 1977; Ničković 1982). With the benefit of hindsight, we feel reinforced in the feeling that this choice has not been a mistake.

In simulation of the geostrophic adjustment process, the *B/E* grid has a grid-separation problem with the external and the lower internal modes for short waves. However, a technique has been developed (Mesinger 1973; Janjić 1979) that, to a large extent, overcomes this problem (Vasiljević 1982; Cullen 1983; Janjić and Mesinger 1984). The *C* grid, on the other hand, has difficulty with higher internal modes, for *all* wavelengths. These modes are present in models with currently used vertical resolutions and it is not known whether something can be done about this problem.

For simulation of the slowly changing quasi-geostrophic motion, horizontal advection schemes that control energy cascade toward smaller scales have been developed for both the *C* and the *E* grid (Arakawa and Lamb 1981; Janjić 1984). However, not all of the conservation properties of the two schemes are the same. Among the differences, the *C* grid scheme conserves *potential* enstrophy, while the *E* grid scheme conserves momentum and imposes a more stringent constraint on the false cascade of energy toward smaller scales. Specifically, within the nondivergent part of the flow, it completely prevents the false cascade of energy into the two-grid-interval wave. Thus, on balance, properties of the *E* grid scheme do not appear inferior, and may be superior, to those of the *C* grid scheme.

Finally, a very recent study of Dragosavac and Janjić (1987) shows that, with currently used horizontal res-

olutions, the linear amplitude response of the centered *B/E* grid schemes to forcing by topography may be generally more accurate than that of the *C* grid schemes. Thus, according to this study, the *B/E* grid may be advantageous for the simulation of the steady solutions induced by topography, even on the synoptic scale.

However, both the *C* and the *B/E* grid can be used with the step-mountain approach. Indeed, a successful application of the step-mountain technique in a *C* grid model is being reported by Aragão, of the University of Miami (personal communication). For our part, we have introduced the step-mountain coordinate into the latest version of the *E* grid limited-area model two of us have been developing over a number of years (Mesinger 1977; Janjić 1977, 1979; Mesinger and Strickler 1982; Janjić 1984).

#### *b. Hydrostatic equation and the vertical grid*

Along with a change of the vertical coordinate of the above-mentioned model, a change of the hydrostatic equation appears to be appropriate. Namely, the hydrostatic equation scheme used previously (Janjić 1977) was designed to reduce the pressure gradient force errors due to steep coordinate surfaces and required calculation of an exponential function at every grid point and time step.

Now that the coordinate surfaces are approximately horizontal, this effort seems redundant. Therefore, our hydrostatic equation has been simplified to the following

$$\Delta\Phi = -(RT/\bar{p}^n)\Delta p. \quad (3.1)$$

Here  $\Delta\Phi$  and  $\Delta p$  represent the increments of geopotential and pressure, respectively, across an eta layer.

Specification of the top pressure surface of the model and of the layer thicknesses is needed in order to complete the definition of the vertical grid. In experiments of Mesinger and Strickler, these choices have been based on the hydrostatic equation which now, as pointed out, has been abandoned. With the present hydrostatic equation, the technique that had been used by Mesinger and Strickler was inappropriate. Therefore, for each of our two regions, the top pressure surface of the model was chosen to coincide with the highest pressure level for which analyses were available. These levels were 10 mb for the European region and 20 mb for the North American region.

For the European region, nine standard "GFDL" layer thicknesses (Smagorinsky et al. 1965) were used. For the North American region, experiments were performed both with the nine-layer GFDL and the 16-layer NGM setup.

#### *c. "Silhouette" and "four-point" mountains*

In defining the model mountains, one requirement is similar to that found in the sigma system framework,

namely, the specification of terrain heights so as to adequately represent the barrier effect of real topography (e.g., Mesinger 1977; Wallace et al. 1983). Note should be taken, however, of possible adverse effects accompanying the benefits of mountain enhancement (Tibaldi 1986). With the step-mountain system, additional considerations may be made. For example, a straightforward discretization of "input" grid point terrain elevations to nearest reference interface elevations may produce some temperature points surrounded on all four sides by wall wind points. Such "windless" valleys seem undesirable since they are insufficiently resolved by the horizontal resolution used. Still another consideration we had was a practical one: for expedience and/or comparison against earlier results, rather than use one of the available very high resolution terrain tapes, we wanted to use grid point terrain fields already prepared for earlier experiments or for other models. For these, and two more other reasons explained below, we have chosen the mountain specification procedure consisting of five consecutive steps, which are as follows.

- 1) "Input" grid point terrain heights are prescribed or prepared by space interpolation. For the European region (Alpine lee cyclogenesis) experiments, these have been the mountains used for one of the cases (that of December 1969) by Mesinger and Strickler. They had been obtained after a "valley filling" and an additional moderate envelope-type (0.5 of the standard deviation) enhancement. For our North American region, several different input mountains have been used, as will be described later.

- 2) To avoid creation of isolated temperature points in subsequent discretization steps, terrain elevations are made to be equal for groups of four neighboring terrain points. We have attempted to do this without reducing the barrier effect present in input heights, as would have happened were a simple four-point averaging to be performed. Thus, instead, "silhouette" averaging (Mintz, personal communication) of terrain elevations of the groups of four neighboring points is performed; this is done so as to provide them with an elevation equal to the average height of the silhouette they present to the horizontal airflow. In other words, area-averaging of four neighboring heights is performed in vertical planes, rather than in a horizontal plane. For consistency with the horizontal advection scheme of the model (Janjić 1984), average silhouette heights are first calculated for four orientations of the vertical plane. These are the four orientations normal to each of the grid lines passing through the center of the four-point grid box. The four average silhouette heights are then averaged, using weights  $\frac{2}{3}$  and  $\frac{1}{3}$  as appropriate in view of the mentioned advection scheme of the model.

As an exception to this four-point averaging, if two or more of the four input points happen to be over the sea, the four-point box is defined to represent a sea

box. This is done in order to prevent spreading of continents, as happened, for example, with the ad hoc procedure used by Bleck (1977).

Each of the four-point grid boxes has a wind point in its center and is discretized in the steps to follow to the same reference interface elevation. Hence, the possible appearance of isolated temperature points is precluded.

One might be concerned about the loss of detail through this four-point grouping of the terrain points. On the other hand, it may be that the forcing within the "4 to 2  $\Delta x$ " scale, to the extent that can easily be avoided, is not desirable in a grid point model because of the aliasing and other errors that occur in that range. Thus, the four-point grouping may be beneficial, irrespective of the considered step-mountain issue of isolated temperature points. It should be stressed, however, that the four-point averaging is by no means required by the finite-difference schemes used in the model and need not be done if one prefers not to do so. Alternative procedures of preventing the creation of isolated temperature points could be devised.

As already pointed out, a separate definition of single-grid-point input terrain heights done within step 1 has been followed here for practical reasons; in other words, it was not meant to serve the interests of the representation of mountains. Ideally, with very high resolution terrain data available, silhouette averaging would have been performed immediately on the four-point mountain boxes, without going through the step 1 listed here.

The silhouette aspect of the four-point grouping discussed here was, of course, only a special case of a problem of arriving at elevations preserving the barrier effect present in given higher resolution terrain data. Lately, this problem was typically handled by the introduction of the so-called envelope orography (Wallace et al. 1983, Tibaldi 1986). The silhouette averaging should be distinctly superior, since it is based on the actual and not on an assumed shape of the higher resolution terrain. Specifically, the envelope technique assumes a biharmonic shape of subgrid-scale mountains. With the actual shape of subgrid-scale orography known, there is no reason to make an assumption about this shape. Examples are easily found of shapes for which the envelope technique is clearly inappropriate. Thus, a plateaulike mountain of a scale larger than the grid scale—not a rare shape among real world mountains—may through the envelope procedure acquire awkward fencelike additions along its edges. Indeed, this has been noticed to happen in the case of Tibet (Manabe, personal communication). The silhouette averaging leaves such a mountain essentially unchanged, just as one would wish to have it.

3) Discretization is performed to the nearest of the elevations the model interfaces would have if pressure were equal to the reference pressure, chosen to be the standard atmosphere. For the European region, with

the top pressure and layer thicknesses as stated, this has resulted in interface elevations of 0, 290, 1112, 2433, . . . ,  $m$ .

4) Substantial mountain gaps (saddle points) are restored if these have been closed in the preceding two steps. The idea underlying this effort is the possibility that in discretization done on a four-point by four-point basis, gaps might be closed between mountains that one would not have wanted closed considering the original higher resolution ("input") terrain field. Details of this procedure will be omitted here; essentially, they required the saddle shape to have been of a sufficient "amplitude" defined in terms of the reference layer thickness. For our European region, the gap restoration rules, as defined, have restored one four-point mountain gap, that between the Pyrenees and the Alps.

5) Finally, in our experiments, four-point mountain boxes are removed that happen to be located, completely or partially, in a given number of the outermost rows of grid points along the boundaries of the model domain. The number of "no-mountain" lines was six for the European region and five for the North American region experiments.

For our European region, the described procedure resulted in the mountains shown in Fig. 2. It should be noted that the terrain height contours shown in the figure are obtained using a code that involves a standard space interpolation scheme resulting in some deformation and shifting of lines relative to their actual position. Without this shifting, the three contours printed would have touched at the southernmost point of model Alps, where the eta model terrain heights form a vertical edge rising from sea level through all three of the lowermost model layers, that is, up to the height of 2433 m.

#### 4. Internal boundaries

The steplike mountains introduce the problem of internal boundaries between the free atmosphere and the mountain blocks. This problem is related only to horizontal differencing. Therefore, it is sufficient to consider a barotropic fluid. In addition, for simplicity, it is convenient to use the plane geometry.

As the first step, the locations of the mountain blocks should be specified. We have chosen the height points, assuming that the blocks fill entire grid boxes. On the Arakawa *E* grid displayed in Fig. 3, an example of grid boxes filled with mountains is shown, with the mountains indicated by shading. As usual, the symbol  $h$  in the figure denotes the height of the free surface, and  $d$  is the distance between the two nearest grid points carrying the same variable. As stated in the preceding section, groups of four neighboring points are assumed to have the same elevation, so that the mountain shown is our "minimum" model mountain. It should be stressed, however, that this choice has been made for

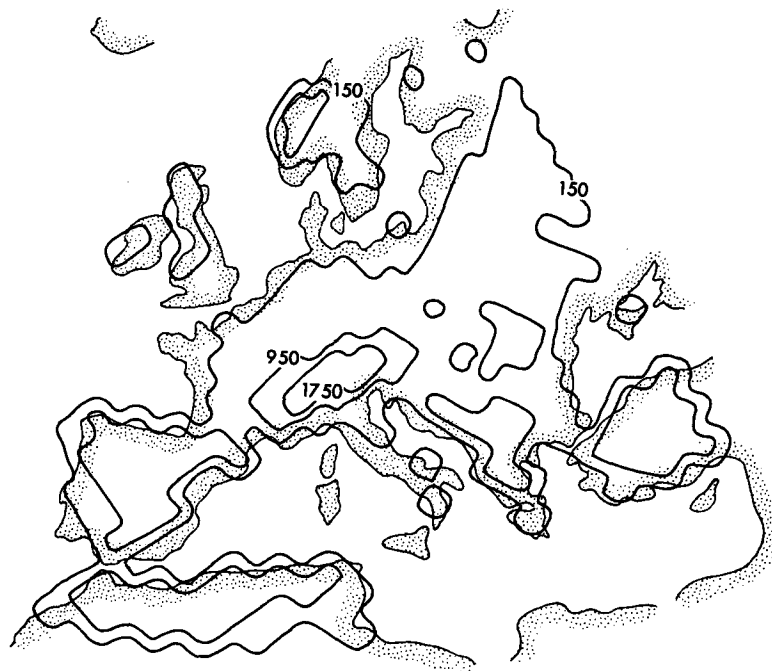


FIG. 2. Terrain heights obtained for the European region, following steps 1 through 5. Steps at 290, 1112, and 2433 m; shown with contours at 150, 950, and 1750 m.

reasons other than the internal boundary scheme formulation, and that the analysis of this section will, in fact, be applicable to mountains formed of an arbitrary number of neighboring height points, including single ones.

At the velocity points located along the internal boundaries we choose the no-slip boundary condition, i.e.,

$$\mathbf{v} = 0. \quad (4.1)$$

In the text to follow, properties will be examined of horizontal advection schemes obtained when fictitious velocity points are introduced inside the mountains at places where velocity points would be located if the mountains were absent. At these points we assume that

$$\mathbf{v}_{\text{ground}} = 0. \quad (4.2)$$

In order to check whether, and if so to what extent, the internal boundaries affect the conservation properties of the advection schemes used in the model, it is convenient to start with a review of several relevant properties of the  $E$  grid. Following Janjić (1984), the velocity field on the  $E$  grid can be represented in terms of the streamfunction  $\psi$  and velocity potential  $\chi$ , as shown in Fig. 4. Note, furthermore, that an Arakawa staggered  $C$  grid can be introduced with the  $\psi$  points coinciding with those of the  $E$  grid; this, in fact, has been done to arrive at the advection scheme that will be considered here. Two coordinate systems— $x, y$  and  $x', y'$ —rotated for  $45^\circ$  with respect to each other, are

also introduced in the figure. The rotational velocity components on the semistaggered grid  $E$ , and on the staggered grid  $C$ , can be defined applying the operator

$$\delta_s \psi = [\psi(s + \Delta s/2) - \psi(s - \Delta s/2)]/\Delta s, \quad (4.3)$$

along the coordinate axes  $x, y$  and  $x', y'$ . The increment  $\Delta s$  in (4.3) takes on the value  $\sqrt{2}d$ , or  $d$ , depending on whether the operator is applied along the coordinate axes  $x, y$ , or  $x', y'$ .

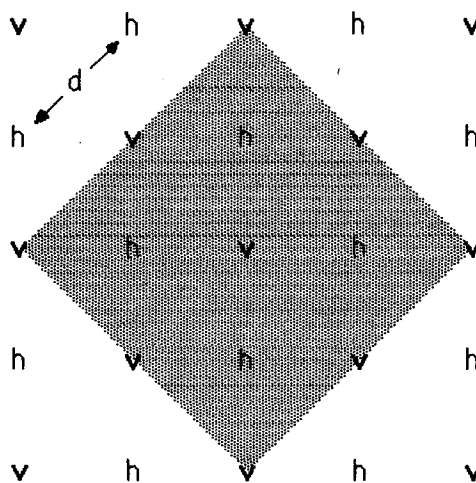


FIG. 3. Grid  $E$  with "minimum-extension" four-point step-mountain indicated by shading. Distance between two nearest grid points carrying the same variable is denoted by  $d$ .

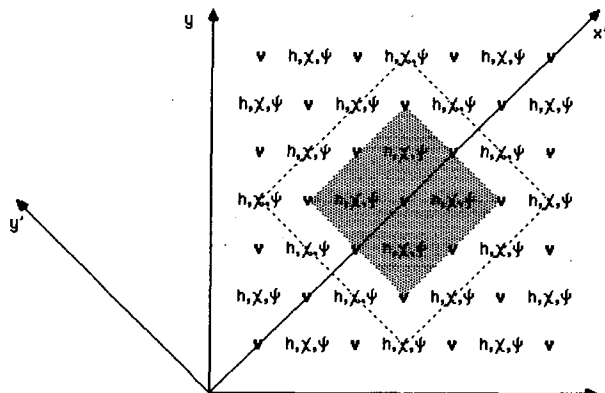


FIG. 4. Grid *E* with streamfunction  $\psi$  and velocity potential  $\chi$  grid points used to define the velocity components along the coordinate axes  $x$ ,  $y$  and  $x'$ ,  $y'$ . The mountain blocks are indicated by shading. The constant  $\psi$  area is bounded by the dotted line.

It should be noted that in the case of nondivergent flow, (4.1) and (4.2) will be satisfied if the streamfunction is constant at the fictitious points inside the mountain and at the row of  $\psi$  points in the free atmosphere next to the mountain. We shall assume this to be the case. The area of constant streamfunction is indicated in Fig. 4 by the dotted line.

As can be seen from Fig. 4, rotational velocity components in the sense of the *C* grid are located midway between the nearest  $\psi$  points and have the form

$$u'_r = -\delta_y \psi, \quad v'_r = \delta_x \psi.$$

On the *E* grid the rotational velocity components are defined by

$$u_r = -\delta_y \psi, \quad v_r = \delta_x \psi.$$

Note that within the constant  $\psi$  area, the rotational velocity components, as well as the *C* and *E* grid finite-difference analogues of vorticity are equal to zero.

The conservation properties of the horizontal finite-difference schemes are achieved through mutual cancellation of the fluxes between the neighboring points. With the step-mountain approach, this cancellation cannot be accomplished in the entire integration domain because some of the grid points do not have all of the neighboring points required for the cancellations. In this situation, conservation will nevertheless be achieved if the uncompensated fluxes are equal to zero. This will be the case if either of the following two conditions is satisfied:

- (i) The velocity component entering the flux definition is equal to zero; or
- (ii) The quadratic quantity appearing in the flux definition is defined as a product of the values at two neighboring grid points and vanishes because the value at the fictitious grid point inside the mountain, or at the points along the side of the mountain, is equal to zero.

The Janjić (1984) *E* grid horizontal advection scheme conserves the mean enstrophy, vorticity, and rotational energy as defined on the staggered grid *C*. In the case of nondivergent flow, using the *E* grid rotational velocity components  $u_r$  and  $v_r$  for the definition of the fluxes, these quantities are governed by the equations

$$\begin{aligned} \partial(\zeta'^2/2)/\partial t = & -\frac{1}{3} \{ \delta_x [u_r \overline{\zeta' \zeta'}^x / 2] + \delta_y [v_r \overline{\zeta' \zeta'}^y / 2] \} \\ & -\frac{2}{3} \{ \delta_x [(\sqrt{2}/2)(\overline{u_r + v_r})^{y'} \overline{\zeta' \zeta'}^{x'} / 2] \\ & + \delta_y [(\sqrt{2}/2)(\overline{-u_r + v_r})^{x'} \overline{\zeta' \zeta'}^{y'} / 2] \}, \end{aligned}$$

$$\begin{aligned} \partial \zeta' / \partial t = & -\frac{1}{3} \{ \delta_x [u_r \overline{\zeta'}^x] + \delta_y [v_r \overline{\zeta'}^y] \} \\ & -\frac{2}{3} \{ \delta_x [(\sqrt{2}/2)(\overline{u_r + v_r})^{y'} \overline{\zeta'}^{x'}] \\ & + \delta_y [(\sqrt{2}/2)(\overline{-u_r + v_r})^{x'} \overline{\zeta'}^{y'}] \}, \end{aligned}$$

$$\begin{aligned} \partial(u_r'^2/2)/\partial t = & -\frac{1}{3} \{ \delta_x [\overline{u_r' u_r'}^x / 2] + \delta_y [\overline{v_r' v_r'}^y / 2] \} \\ & -\frac{2}{3} \{ \delta_x [(\sqrt{2}/2)(\overline{u_r + v_r})^{y'} \overline{u_r' u_r'}^{x'} / 2] \\ & + \delta_y [(\sqrt{2}/2)(\overline{-u_r + v_r})^{x'} \overline{u_r' u_r'}^{y'} / 2] \} + \dots, \end{aligned}$$

$$\begin{aligned} \partial(v_r'^2/2)/\partial t = & -\frac{1}{3} \{ \delta_x [\overline{u_r' v_r'}^x / 2] + \delta_y [\overline{v_r' v_r'}^y / 2] \} \\ & -\frac{2}{3} \{ \delta_x [(\sqrt{2}/2)(\overline{u_r + v_r})^{y'} \overline{v_r' v_r'}^{x'} / 2] \\ & + \delta_y [(\sqrt{2}/2)(\overline{-u_r + v_r})^{x'} \overline{v_r' v_r'}^{y'} / 2] \} + \dots. \end{aligned}$$

Here,  $\zeta'$  is the vorticity as defined on the *C* grid, and the expressions of the form  $\overline{AA}^s$  represent the products of the values of  $A$  at two neighboring grid points along the axis  $s$ .

Direct inspection of the above equations reveals that at the internal boundaries, the *C* grid enstrophy is conserved because both conditions (i) and (ii) are satisfied; vorticity, and therefore *C* grid rotational momentum, is conserved because condition (i) is satisfied; and, finally, the *C* grid rotational energy is conserved because condition (ii) is satisfied.

If the divergent part of the flow is included, the continuity equation, the equations governing the evolution of the kinetic energy as defined on the *E* grid under the advective processes, and the *E* grid momentum equations have the form (Janjić 1984):

$$\partial h / \partial t = -\left\{ \frac{1}{3} (\delta_x U + \delta_y V) + \frac{2}{3} (\delta_x U' + \delta_y V') \right\},$$



$$\begin{aligned}
\partial(\bar{h}^x u^2/2)/\partial t &= -\left\{\frac{1}{3} [\delta_x(\bar{U}^x \bar{u}^x/2) + \delta_y(\bar{V}^x \bar{u}^x/2)] \right. \\
&\quad \left. + \frac{2}{3} [\delta_x(\bar{U}'^x \bar{u}'^x/2) + \delta_y(\bar{V}'^x \bar{u}'^x/2)]\right\} + \dots, \\
\partial(\bar{h}^y v^2/2)/\partial t &= -\left\{\frac{1}{3} [\delta_x(\bar{U}^y \bar{v}^y/2) + \delta_y(\bar{V}^y \bar{v}^y/2)] \right. \\
&\quad \left. + \frac{2}{3} [\delta_x(\bar{U}'^y \bar{v}'^y/2) + \delta_y(\bar{V}'^y \bar{v}'^y/2)]\right\} + \dots, \\
\partial(\bar{h}^x u)/\partial t &= -\left\{\frac{1}{3} [\delta_x(\bar{U}^x \bar{u}^x) + \delta_y(\bar{V}^x \bar{u}^x)] \right. \\
&\quad \left. + \frac{2}{3} [\delta_x(\bar{U}'^x \bar{u}'^x) + \delta_y(\bar{V}'^x \bar{u}'^x)]\right\} + \dots, \\
\partial(\bar{h}^y v)/\partial t &= -\left\{\frac{1}{3} [\delta_x(\bar{U}^y \bar{v}^y) + \delta_y(\bar{V}^y \bar{v}^y)] \right. \\
&\quad \left. + \frac{2}{3} [\delta_x(\bar{U}'^y \bar{v}'^y) + \delta_y(\bar{V}'^y \bar{v}'^y)]\right\} + \dots.
\end{aligned}$$

Here,

$$\begin{aligned}
U &= \bar{h}^x u, \quad V = \bar{h}^y v, \quad U' = \bar{h}^{x'} (\sqrt{2}/2)(\bar{u} + \bar{v})^{y'}, \\
V' &= \bar{h}^{y'} (\sqrt{2}/2)(-\bar{u} + \bar{v})^{x'}.
\end{aligned}$$

Again, direct inspection reveals that the mass is conserved because the condition (i) is satisfied, and the  $E$  grid kinetic energy is conserved because the condition (ii) is satisfied. However, the  $E$  grid momentum is not conserved. We decided not to look for another definition of boundary conditions and therefore did not try to enforce the momentum conservation. Possible detrimental effects, if any, were not noticed in the experimental integrations we have performed so far.

An important process that cannot be treated within the frame of the barotropic model is the temperature advection. However, all relevant information can be obtained by examining the properties of the scheme for the advection of a passive quantity  $T$ , carried at  $h$  points. The scheme for temperature advection used in the model, combined with the continuity equation, takes the form

$$\begin{aligned}
\partial(hT)/\partial t &= -\left\{\frac{1}{3} [\delta_x(U\bar{T}^x) + \delta_y(U\bar{T}^y)] \right. \\
&\quad \left. + \frac{2}{3} [\delta_x(U'\bar{T}'^x) + \delta_y(V'\bar{T}'^y)]\right\}.
\end{aligned}$$

Direct inspection reveals that the condition (i) is satisfied and therefore the first moment of the distribution of  $T$  is conserved. Multiplying this equation by  $T$ , and taking into account the continuity equation, one easily finds that the second moment is also conserved, again because the condition (i) is satisfied.

Thus, with the internal boundary conditions specified as above, except for the  $E$  grid momentum, all favorable conservation properties of the Janjić (1984)  $E$  grid advection schemes are preserved.

Another internal boundary problem we have looked into is that of the mass conservation within the modification of the continuity equation designed to suppress the  $E$  (or  $B$ ) grid two-grid-interval noise (Mesinger 1973; Janjić 1979). As this modification, the term proportional to

$$-(\nabla_x \cdot \mathbf{P}' - \nabla_y \cdot \mathbf{P}) \quad (4.4)$$

is added to the right-hand side of the surface pressure tendency equation. Here  $\nabla_x \cdot$  and  $\nabla_y \cdot$  are the divergence operator analogs, and  $\mathbf{P}'$  and  $\mathbf{P}$  pressure gradient force analogs, calculated along the axes  $x, y$  and  $x', y'$ , respectively (Janjić 1979; see also Cullen 1983).

In our model, however, (4.4) is replaced by

$$-\frac{1}{2}(\bar{\Pi}^x - \bar{\Pi}^y), \quad (4.5)$$

where

$$\Pi \equiv \delta_{x'} P_{y'} + \delta_{y'} P_{x'}.$$

Note that with pressure gradient force a potential vector, as, for example, in the simple shallow water case, there is no difference between the analogs (4.4) and (4.5).

A term proportional to (4.5) at a height point consists of contributions proportional to values of  $\Pi$  at four neighboring velocity points. With no internal boundaries, and inside the integration region, these contributions from velocity points are added to values of surface pressure at two of the four surrounding height points. At the remaining two of the surrounding height points, they are subtracted from the values of surface pressure. Thus, no false change of mass will occur due to the addition of a term proportional to (4.5) to the surface pressure tendency equation.

To maintain mass conservation with internal boundaries present, we have set values of  $\Pi$  equal to zero at all velocity points located at the sides of mountains. A similar procedure is used to maintain mass conservation at the lateral boundaries of the integration region. To this end, values of  $\Pi$  are set to zero along the first (outermost) row of velocity points of the integration domain of the model. This is the first row of points following the two rows of points that are used for specification of the lateral boundary conditions of the model.

## 5. The Genoa cyclogenesis experiments

For initial experimental testing of the step-mountain approach we chose to rerun some of the earlier real data integrations of Mesinger and Strickler (1982). Experiments were performed using the same integration region and the horizontal grid, consisting of  $101 \times 37$  points (carrying the same variable), located at every other intersection of a  $0.75^\circ \times 0.50^\circ$  longitude  $\times$  latitude mesh.

Since a comparison against earlier results could be of some interest, it may be helpful to summarize the differences between the present model and that used for the integrations of the previous paper. As pointed out, the present model has a code option to be run as an "eta" and as a sigma system model. In its sigma "mode," it contained the following changes compared to that of Mesinger and Strickler (1982).

- The horizontal advection scheme of Janjić (1984) was used, achieving a strict control of false energy cascade toward smaller scales.

- The finite-difference hydrostatic equation (3.1) was used. As a result, as explained in section 3b, some differences in the distribution of layer thicknesses and in the location of the top pressure surface were introduced.

- A simple second-degree horizontal diffusion code only was available, with no option to use the fourth-degree diffusion. A conversion relation between the two diffusion coefficients was used, designed to give the same rate of change for single grid point perturbations of the diffusing quantity. The difference between the two schemes, however, should have been of an exceedingly little effect since a sensitivity experiment performed has shown that the coefficient chosen resulted in changes on 48 h output maps that were almost impossible to notice. Thus, horizontal diffusion was almost completely absent, in the present as well as in the previous experiments. In addition, again inadvertently, the nine-point smoothing previously performed on sea level pressure maps for points with terrain elevations above 1000 m was omitted.

Regarding other model details, recall that the scheme used to conserve energy in transformations between the kinetic and potential energy is given in the Appendix. "Physics" of the model was of the typical simple ("dry") type, with surface drag, elevation dependent over land; surface velocity dependent over ocean; parameterized vertical momentum transport; and the standard dry convective adjustment. For more details on features of the model not different from those of the model used by Mesinger and Strickler, the reader is referred to their paper.

Mountain/no mountain experiments done with the four cases simulated by Mesinger and Strickler have shown that cyclogenesis resulting from the existence of mountains occurs in only two of the cases. These two cases, from December 1969 and April 1973, were chosen for the present experiments. Of various sensitivity experiments performed with these cases, two have been done with both the eta and the sigma mode option, keeping all other parameters the same.

The December 1969 eta/sigma mode experiment was performed starting from the same initial conditions as the simulations of Mesinger and Strickler, and for the same integration period of 48 h. Sea level pressure and 500 mb height maps of that case are shown as upper left panels in Figs. 6 and 7 of their paper. As for

these previous simulations, boundary conditions were prescribed by linear time interpolation of the observed fields, analyzed at 24 h intervals. Resulting sea level pressure maps are shown in Fig. 5. For reasons of convenience, the region shown on maps (including the map of the step-mountains used, Fig. 2) is on each side one grid line smaller than the actual integration region, extending from 30° to 66°N and from 35°W to 40°E.

In obtaining the maps shown, pressure reduction to sea level was not done at places where the ground elevation of at least one of the four points used for space interpolation was higher than 2000 m. This area is shaded by dots. Another feature of the map code that should be mentioned is that contours were plotted following character fields originally prepared for line-printer-type shaded maps. This has resulted in some enhancement of the small-scale noise, as seen, for example, along the southern boundaries of the two maps. (Note that this noise is smaller in scale than the model grid distance, 81 km at 45° lat, defined as the distance between points carrying the same variable.)

Noticeable differences in the two maps can be seen at the low-pressure centers east of the Scandinavian mountains and in the lee of the Alps, as well as along the trough connecting these two centers. In the eta mode map (lower panel), the low centered over the Gulf of Finland, the so-called parent low of the Genoa lee cyclone, has two closed contours less than that of the sigma mode map (upper panel). The central pressure of that low on the eta mode map is approximately correct according to available synoptic observations (e.g., *Täglicher Wetterbericht*, published by Deutscher Wetterdienst, Offenbach/Main, FR Germany). More intensive ridging between the two lows on the eta mode map, possibly indicating an enhanced flow around, rather than over, the Alps also agrees better with observations. Observations, in fact, show a still more intense ridging. The weaker lee cyclone of the eta experiment, on the other hand, is not an improvement compared to observations, as they indicate the minimum sea level pressure of the lee cyclone at the considered verification time as low as about 990 mb. Results displayed in Fig. 5 should not be understood as indicating a tendency of the eta integrations to result in generally weaker low centers: the second eta/sigma mode experiment, to be shown later, gave the eta mode lee cyclone by approximately the same amount deeper than that of the sigma mode run. It may also be recalled that only a "minimum physics" type of a model was used, with, for example, no radiation and no latent heat release.

The sensitivity of the sigma versus eta formulation, revealed by the two maps in pressure differences of up to several millibars, would seem to be significant in view of the reasonably high resolution used for the present experiment.

Comparison of the two maps shown in Fig. 5 may also be revealing a higher level of noise in the sigma

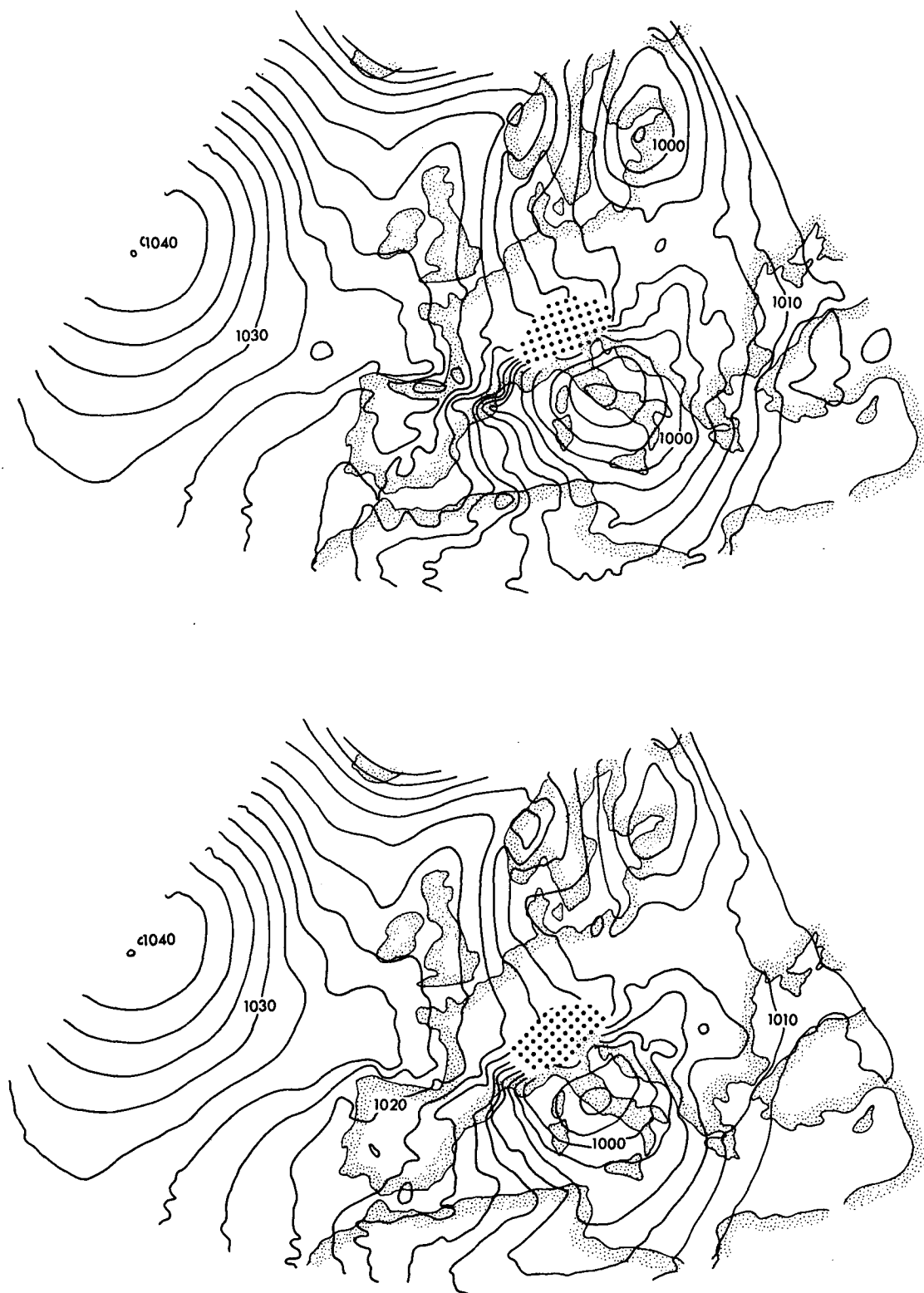


FIG. 5. Sea level pressure maps obtained in 48 h simulations using the sigma system (upper panel) and the "eta" system (lower panel). Contour interval is 2.5 mb; see text for other details.

simulation. The isobars of the sigma mode map over the Iberian Peninsula are clearly noisier than those of the eta mode map. Asia Minor, with two closed isobars on the sigma mode map, may be another example.

Because of the pressure reduction required, sea level pressure over mountainous regions may not be the most appropriate indicator of the possible difference in noisiness of the two simulations. Therefore, geopotential height and temperature maps for levels 300, 500 and 700 mb were visually inspected. At all of these levels, sigma mode maps were noisier than the eta mode maps. The difference is particularly striking at the 300 mb level, as can be seen on maps shown in Fig. 6. In this figure, geopotential height maps are shown as upper panels, and temperature maps as lower panels. Both the height and the temperature field of the sigma mode simulation (left-hand panels) are visibly noisier than the corresponding fields of the eta mode simulation (right-hand panels).

A maximum intensity near the tropopause level of the noise generated in the sigma system presumably due to the pressure gradient force error is consistent with the present understanding of this error, as summarized in the introductory section. Specifically, at the uppermost of the three levels considered, the lapse rate would be expected, at most places, to change more with height than at the other two levels, resulting in larger pressure gradient force errors.

Of the experiments performed on the April 1973 case, one deserves more emphasis because of its verification aspect. Recall that it is the detailed analysis of this deep Genoa cyclogenesis by Buzzi and Tibaldi (1978) that has revealed a number of features that have remained in the focus of interest in subsequent numerical and analytical work on the lee cyclogenesis phenomenon. Foremost among those may be the difference between the time and space scale characteristics of the low level lee development and the associated midtropospheric cutoff. As later pointed out by Tibaldi (1980), this distinction seems to be supported by the results of numerical experimentation. Namely, in a number of simulations performed by that time and also so far, a great deal of realism has been achieved in reproducing the small-scale near-surface features of the observed developments (e.g., Bleck 1977; Mesinger and Strickler 1982; Dell'Osso and Radinović 1984). However, it would appear that, as yet, no evidence has been presented of a satisfactory simulation of the midtropospheric cutoff in a case when cyclogenesis was demonstrated to be due to the existence of the mountain obstacle.

Hoping for progress in this area, with the April 1973 case we have performed an integration starting with the analyses of the same time as that of the initial analyses published by Buzzi and Tibaldi, 1200 UTC 2 April. Note that this initial time follows by 24 hours the initial time chosen by Mesinger and Strickler for their simulation of the April 1973 case. At the same time, it is

the earlier of the two 12-h apart initial times that have been used for this case in simulations of Bleck (1977).

Sea level pressure and 500 mb geopotential height maps of our initial fields are shown as the upper left-hand and the lower left-hand panels in Fig. 7, respectively. In addition, sea level pressure and 500 mb height analyses of Buzzi and Tibaldi for the same time are shown in the right-hand panels of the figure. The two Buzzi-Tibaldi maps are slanted for viewing convenience, to have their central meridian ( $2.5^{\circ}\text{E}$ ) the same as that of the initial data maps. As one can see, according to the analysis of Buzzi and Tibaldi, at the initial time the surface front was clearly upstream of the Alps and not yet deformed by the existence of the mountain obstacle. Indeed, sea level pressure and 500 mb height maps of a 36 h simulation without mountains started with the initial fields of the left-hand panels of Fig. 7 (Fig. 8) show only a deep "parent low" and no cyclone over southern Europe. This confirms the expectation that fields of the present initial time still do not contain the mountain-produced deformation needed to set off cyclogenesis in the lee of the Alps.

The same two maps obtained in the simulation using the eta system and mountains of Fig. 2 are shown as left-hand panels of Fig. 9. Observed sea level pressure of the same time, 0000 UTC 4 April, and as analyzed by Buzzi and Tibaldi, is shown as the upper right-hand panel of the figure. The Buzzi-Tibaldi map is again slanted to achieve the same orientation as that of the simulation maps. Since the Buzzi-Tibaldi paper does not contain the 500 mb analysis for this verification time, a section of the "Täglicher Wetterbericht" 500 mb analysis for that time is shown as the lower right-hand panel of the figure. The section covers the same region as the simulation maps, extending from  $30.5^{\circ}$  to  $65.5^{\circ}\text{N}$  and from  $34.25^{\circ}\text{W}$  to  $39.25^{\circ}\text{E}$ .

We find the degree of realism of the simulation maps of this experiment, in particular the cutoff seen on the 500 mb geopotential height map, rather encouraging. An approximately correct depth of the lee cyclone in this 36 h simulation is a visible improvement over the earlier 24 h simulation of Bleck verifying at the same time, shown in his Fig. 11. Depth of the parent low is also correctly simulated. Ridging between the two lows is, however, underpredicted, by close to one contour interval. In agreement with observations, during the 12 h preceding the map time, the simulated lee cyclone moves southeastward along the Adriatic Sea. It is, however, behind the observed cyclone. This appears to be due mostly to its having been formed to the northwest of the observed cyclone, perhaps because of the difference in geometry between the model and the real Alps.

This point on the sensitivity to model mountain geometry is supported by an experiment on the December 1969 case in which the four-point mountains have been centered in a way different from that of Fig. 2. Config-

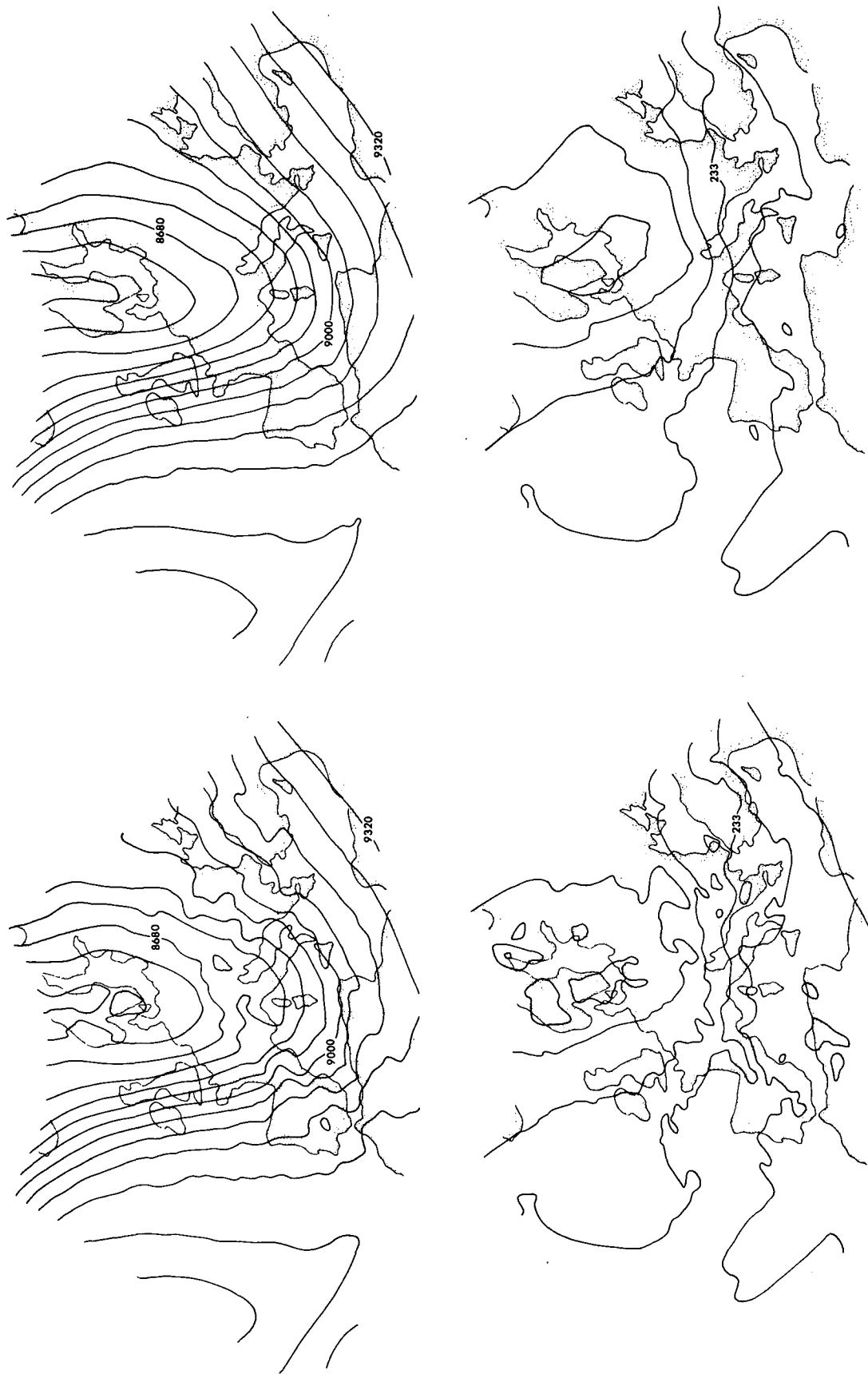


FIG. 6. 300 mb geopotential heights (upper panels) and temperatures (lower panels) obtained in 48 h simulations using the sigma system (left-hand panels) and the eta system (right-hand panels). Contour interval is 80 m for geopotential height and 2.5 K for temperature.

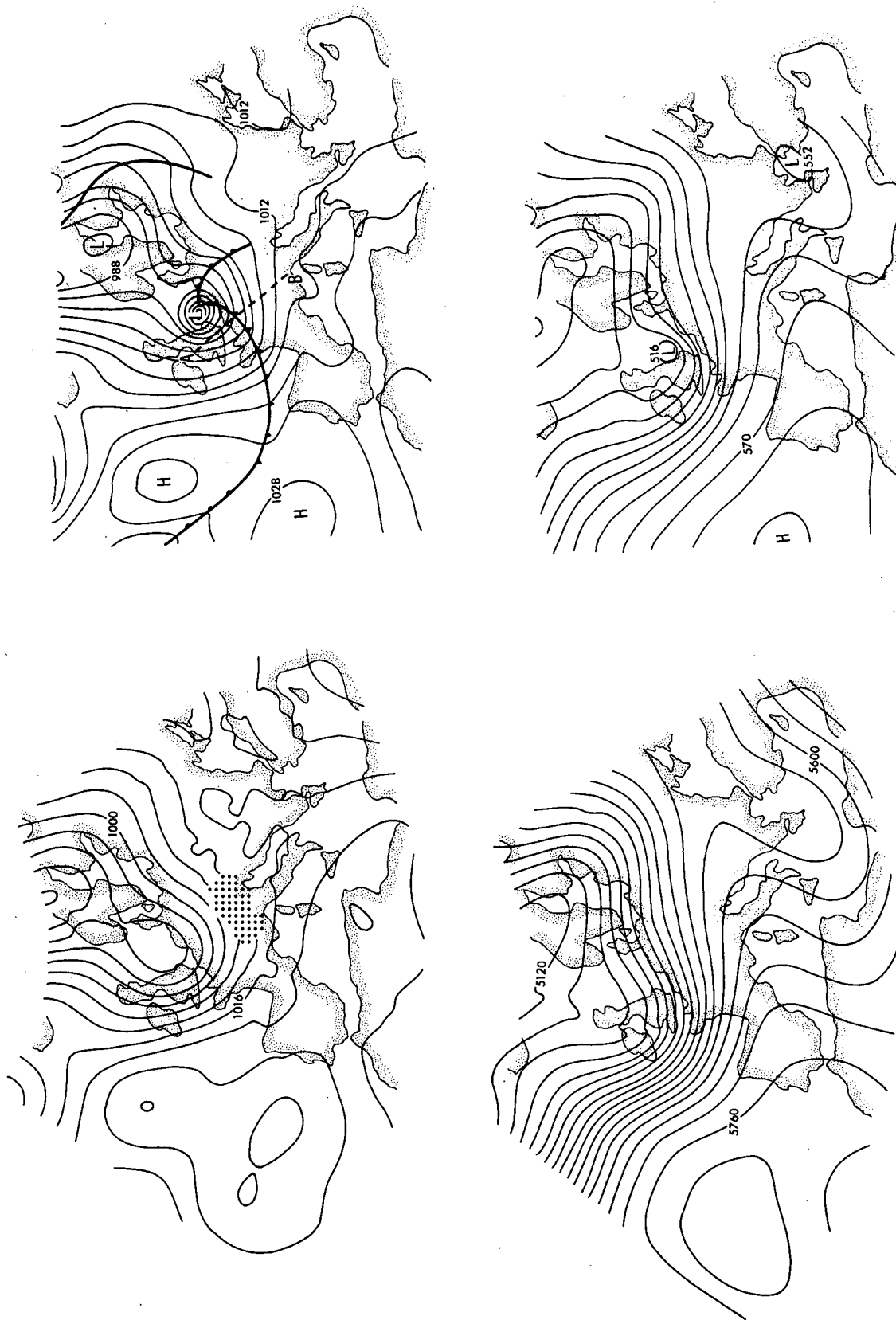


FIG. 7. Sea level pressure (upper left-hand panel) and 500 mb geopotential height (lower left-hand panel) at 1200 UTC 2 April 1973, of the initial condition used to simulate the April 1973 case. The same fields as analyzed by Buzzi and Tibaldi (1978) are shown in the right-hand panels. Contour interval is 4 mb for sea level pressure; for 500 mb heights, it is 40 m for the initial fields map, and 60 m for the Buzzi-Tibaldi map.

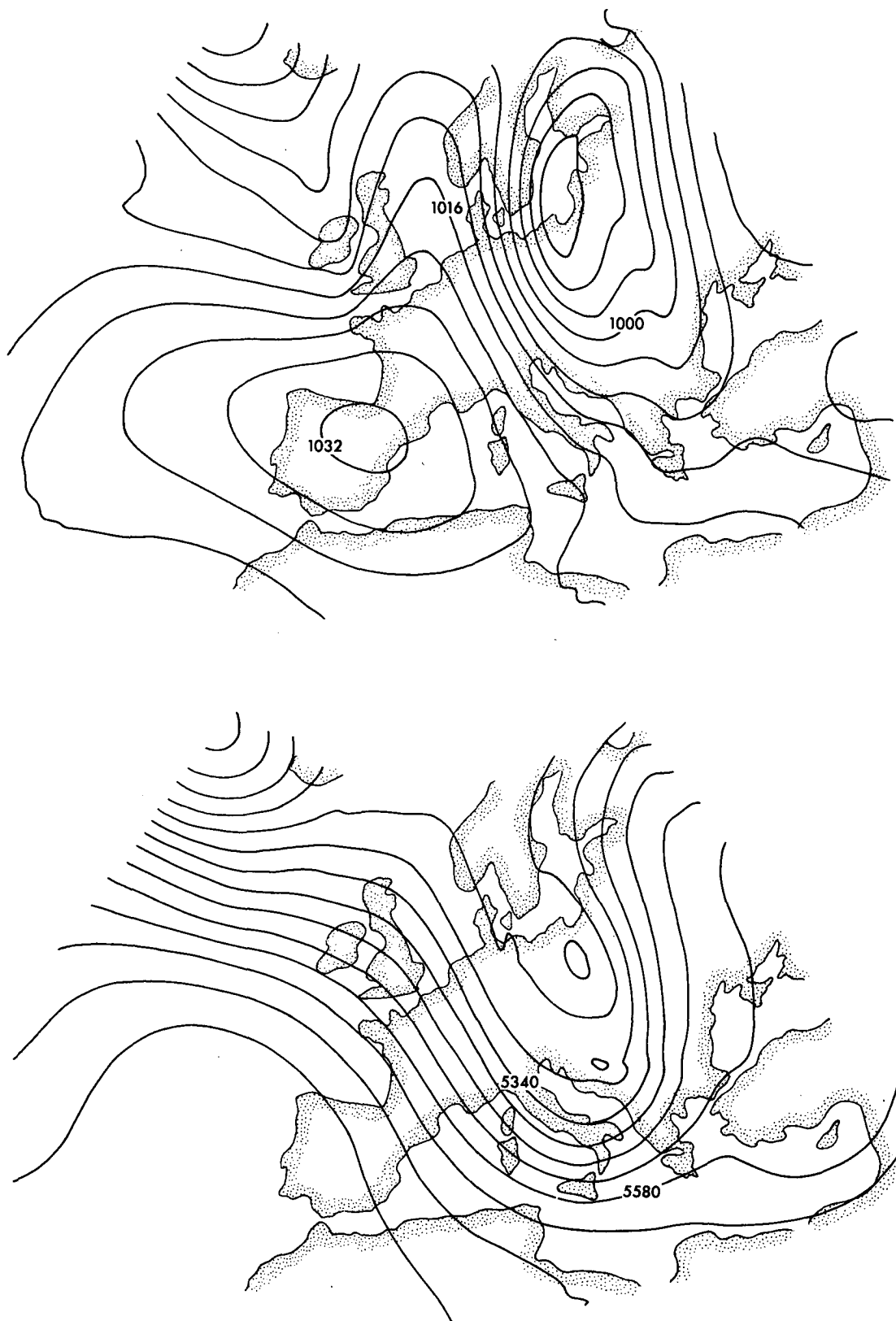


FIG. 8. Sea level pressure (upper panel) and 500 mb geopotential height (lower panel), obtained in a 36 h simulation without mountains, and verifying at 0000 UTC 4 April 1973. Contour interval is 4 mb for sea level pressure and 60 m for geopotential height.

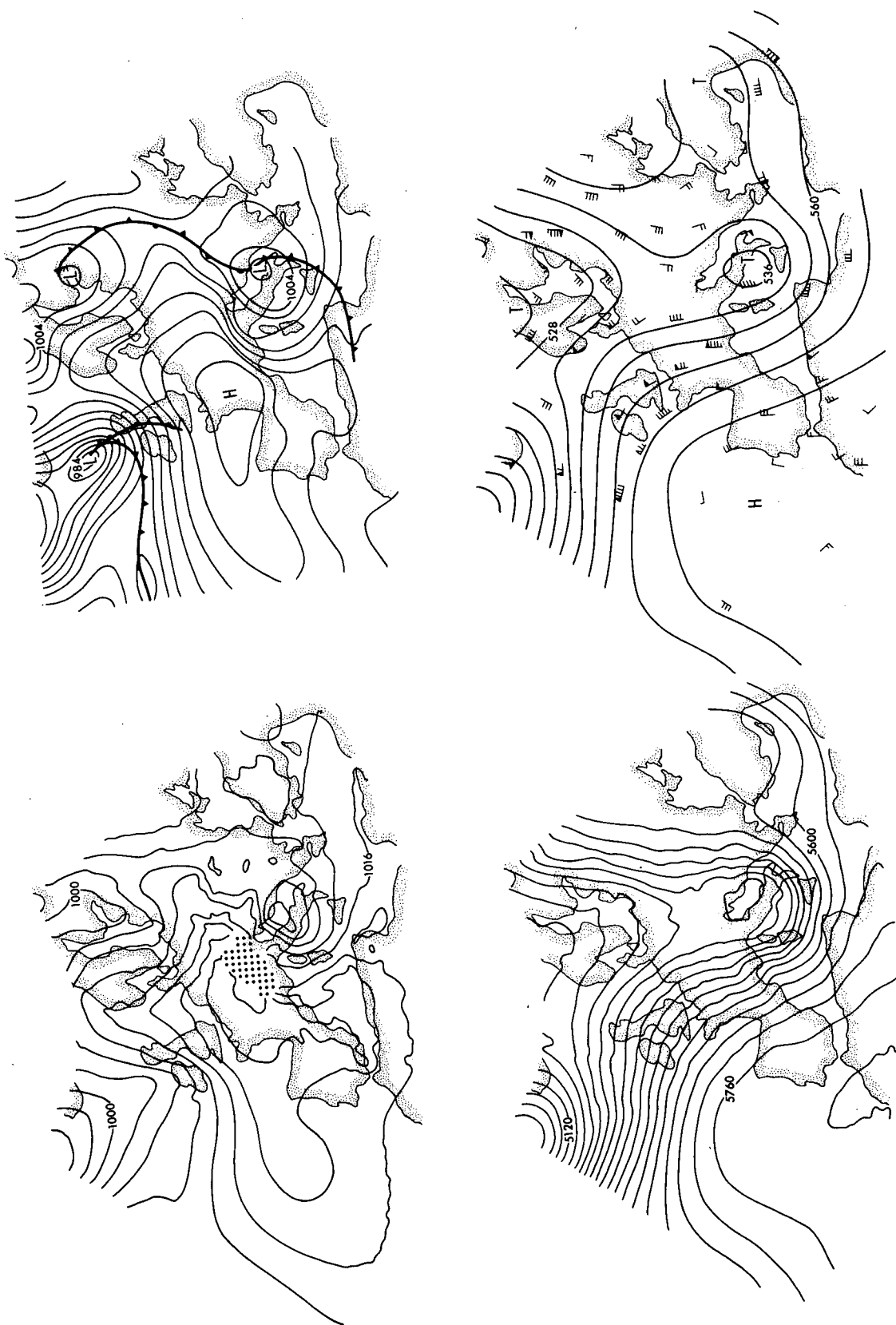


FIG. 9. Left-hand panels—sea level pressure (above) and 500 mb geopotential height (below), obtained in a 36 h simulation with mountains as shown in Fig. 2, and verifying at 0000 UTC 4 April 1973. Right-hand panels—Buzzi-Tibaldi (1978) sea level pressure analysis (above) and 500 mb geopotential height analysis of the German Weather Service (below), for the same time. Contour interval is 4 mb for sea level pressure; for 500 mb heights, it is 40 m for the simulation map, and 80 m for the German Weather Service map.



uration of the lee cyclone visibly different from that shown in the lower panel of Fig. 5 has been obtained with no contour of 995 mb and a two-center shape of the contour of 997.5 mb ("ciclogenesi ad occhiali"—eyeglasses cyclogenesis, Tibaldi, personal communication). Thus, apart from the effects of a more refined boundary layer physics, and of inclusion of latent heat and radiation, further improvement in the realism of the simulation of Genoa cyclogenesis should be possible by a straightforward increase in the resolution of the model, compared to the resolution used here (see also Dell'Osso 1984).

Notwithstanding the remaining inaccuracies, the forecast of Fig. 9 represents an illustration of the partial predictability of mesoscale motions irrespective of the absence, or of the errors in the representation, of the motions of the same scale in the initial data. This is a question receiving increasing attention recently (e.g., Anthes and Kuo 1985), and also with obviously important implications on the ultimate large-scale atmospheric predictability. The initial conditions used in our Genoa cyclogenesis experiments were obtained by space interpolations of the U.S. National Meteorological Center's analyses. For April 1973, these analyses on each pressure level were performed on a stereographic projection, using a grid of 381 km at 60° lat. Analysis involved a repeated application of a smoothing operator, once after each data-fitting scan (McDonnell 1974). The smoothing operator completely eliminated the two-grid-interval wave and had been reducing the amplitude of, for example, the three-grid-interval wave to about 65 percent of its previous value. Thus, at 45° lat, there were no waves left of wavelengths less than 700 km and probably little amplitude left of waves shorter than, say, about 1000 km. Some additional smoothing had to result from space interpolation to a different horizontal grid. Indeed, the initial maps shown in Fig. 7 (left-hand panels) consist of smooth, large-scale features, except for some artifacts of the pressure reduction to sea level (upper left-hand panel) and vertical interpolation (lower right-hand panel). Subjectively analyzed maps for the same time (right-hand panels) do show the presence of smaller scale features. Of particular relevance here is the intensity of the parent low (with the central pressure of 971 mb; Richards and Stubbs 1974), clearly absent in the initial data.

In its initial ("trigger") stage, the Genoa lee cyclone is a rather small-scale phenomenon (e.g., Tibaldi 1980), occupying an area of perhaps about 500 km in diameter. Lack of the initial and also of boundary data information on that scale did not preclude the simulation of the lee cyclone, and neither did it result in the simulated cyclone having space scale features much different from those of the observed cyclone.

An eta/sigma mode experiment was performed also on the April 1973 case; results of both the sigma and the eta mode run of this experiment are shown in Figs. 10 and 11. For more detail in the area of interest, this

time only sections of the maps are shown. The experiment has been performed with model parameters the same as for the preceding figures, except that the horizontal diffusion, found to be of no practical consequence with the coefficient chosen, was absent. In Fig. 10, sections of the sea level pressure maps are shown. On these maps the contour interval is 5 mb, with the contours at 2.5 mb intervals (shown by dashed lines), inserted only when present in regions of minimum pressures. For the maps of Fig. 10, pressure reduction

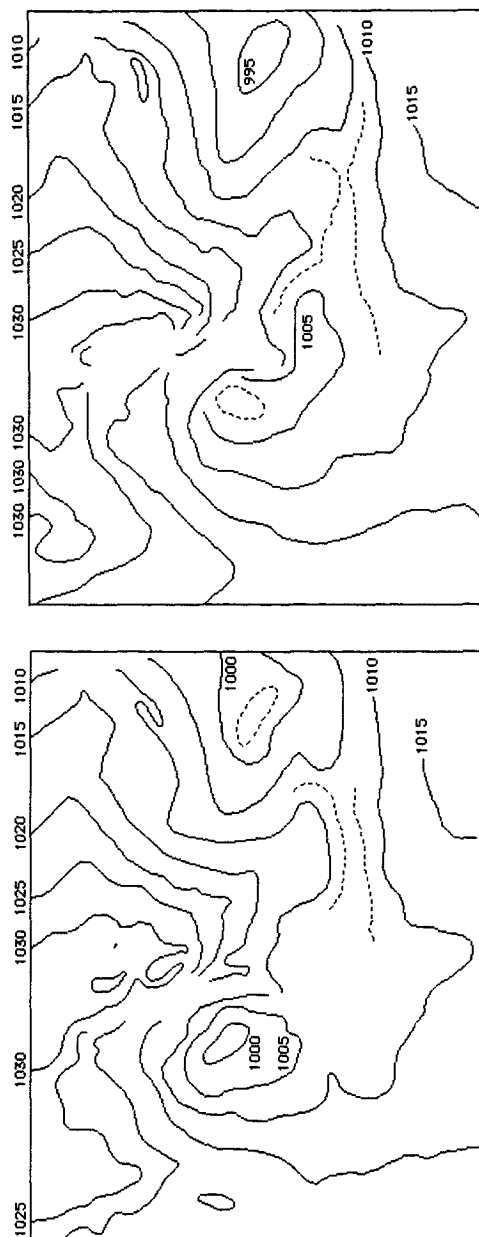


FIG. 10. Sea level pressure maps obtained in 36 h simulations using the sigma system (top panel) and the eta system (bottom panel), verifying at 0000 UTC 4 April 1973. Contour interval is 5 mb; see text for other details.

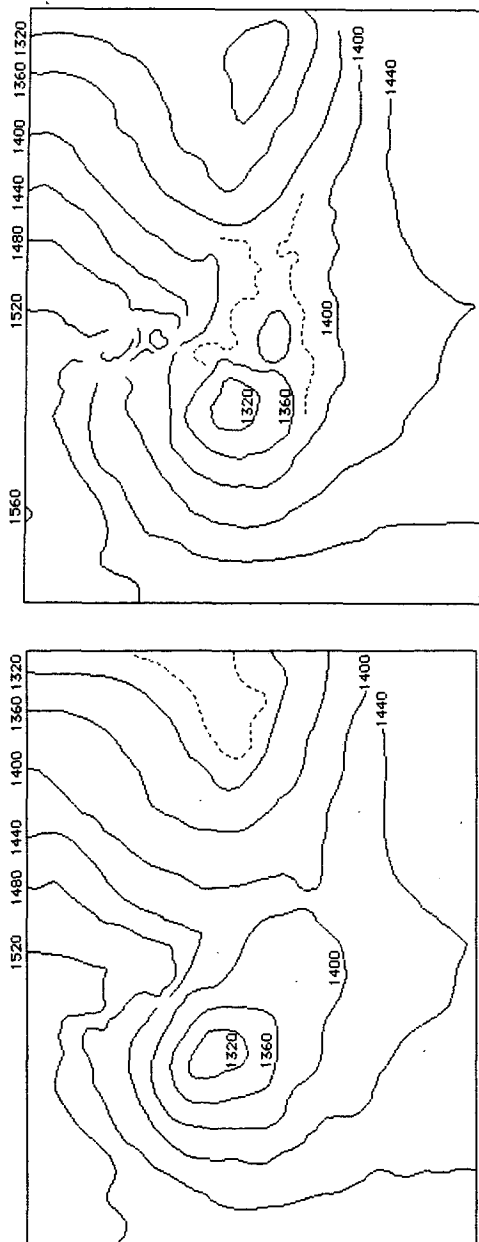


FIG. 11. 850 mb geopotential height maps obtained in 36 h simulations using the sigma system (top panel) and the eta system (bottom panel), verifying at 0000 UTC 4 April 1973. Contour interval is 40 m; see text for other details.

to sea level was not suppressed below high mountains; however, as the maps shown were also derived from line printer maps, a rule was followed to have contours plotted only for a given minimum number of contiguous line printer digits. Thus, contours are discontinued at places where the line printer maps attain a level of noisiness such that this requirement is not met. Continent outlines can be inferred by comparison of the 1000 and 1020 mb isobars of the eta mode map (bottom panel) with these same isobars of the upper left-hand map in Fig. 7.

An insufficiently deep lee cyclone is seen on the sigma mode map (top panel) by about one contour interval. While there is no difference in ridging north of the lee cyclone in terms of isobars that are cut off, one can note that on the side of the advancing cold air the isobars of the eta mode map have progressed farther to the east than the corresponding isobars on the sigma mode map. Thus, there is evidence of an intensified flow around the Alpine barrier. Finally, the sigma mode map is noisier than the eta mode map. The difference is particularly visible in the area of the Alps, in which the higher temperature noise of the sigma mode run results in very erratic fictitious sea level pressure values, and thus in discontinuation of all of the full interval contours present on the section of the map shown. Recall that model parameters provide for no horizontal smoothing or lateral diffusion to reduce the noise as customarily would have been done.

In Fig. 11 geopotential height contours of the 850 mb surface are shown. The full contour interval is 40 m, and the same rules were followed regarding the insertion of half-interval contours and the discontinuation of contours as in the maps of Fig. 10. The lee cyclone of the sigma mode map (top panel) and that of the eta mode map (bottom panel) are, at this level, about the same depth. As there is no appreciable vertical tilt of the axis of the low in the layer between the surface and the considered level, the eta mode cyclone is seen to be warmer than the sigma mode cyclone. Ridging of the trough axis north of the lee cyclone is shown to be more intensive on maps in the eta mode run, which represents an improvement according to observations. Since the trough axis tilts westward, an explanation of this difference between the two runs cannot be made only in terms of the progress of the cold air around the obstacle. Finally, the noisiness of the sigma mode run compared to the eta mode run is more pronounced than at the sea level.

There is not much difference, however, in the progress of the cutoff at the 500 mb level (not shown). Thus, the success in simulation of the midtropospheric cutoff did not come as a result of the step-mountain method. We are of the opinion, therefore, that simulation of the cutoff in this case was successful simply as a result of the generally high accuracy of the simulation of the ridging in the lower troposphere north of the Alps, both in the eta and in the sigma mode runs. As in the December 1969 case, the noisiness of the sigma mode run increases with height and becomes substantial at the mid- and upper troposphere, as illustrated by maps of Fig. 6.

## 6. The Appalachian redevelopment experiment

The objective of our North American region experiments was a comparison against the performance of another sigma system model with roughly the same computational effort in terms of the space resolution as well as the integration region. For convenience, NMC's Nested Grid Model (NGM) was chosen for that

purpose. Therefore, as stated, grid parameters for our North American region were chosen so as to mimic those of the NGM. This is a triply nested model, with about one-third of the computational effort spent on the two outermost grids. Its grid length on the innermost grid, defined on stereographic projection, is 91 km at 60°N. With no nesting, to account for the overhead due to the NGM's outer grids, we have chosen a region resulting from about the same grid distance and with a number of grid points roughly 25 percent higher than that of the NGM's innermost grid. As our code, for efficiency and a more uniform grid geometry, is written in terms of rotated spherical coordinates (Undén 1980; Bates and McDonald 1982; for transformation equations, see Mesinger 1971), we have positioned our grid by choosing the location of its central (height) point; the coordinates chosen were 52.5°N, 100°W. The model region was defined to span 75° × 70° (transformed) longitude × latitude, with grid points at every other intersection of the (15/26)° × (14/26)° transformed longitude × latitude mesh. Thus, the horizontal grid consisted of 8581 height points and 8580 velocity points, about 1.246 times the number of grid points of the NGM's innermost horizontal grid. The choices made resulted in a grid distance varying from 79.6 km at the model's southern and northern boundary to 87.7 km at its central grid line. Also, this made for a region along the model's central meridian extending from 17.5° to 87.5°N (real).

For initial North American region experiments, we have used the GFDL nine-layer vertical structure, as in our European region simulations. For these experiments, for convenience, step mountains were derived from the terrain fields used for the NMC rhomboidal-40 spectral prediction model. Forecasts of this same model were used to prepare the step-mountain model lateral boundary conditions.

Of the so-called special cases (Collins and Tracton 1985) that have been used for comparison of the performance of NGM against that of the NMC Limited-Area Forecast Model (LFM) as "historical cases of meteorological importance," we have looked for cases in which dynamics seemed as a primary or at least a possibly important factor in governing the processes that have attracted interest. In this way, "case 2," and, subsequently, "case 1" have been chosen. For case 2, described by Collins and Tracton as "dramatic cold air plunge into the deep south," NGM forecast was subjectively ranked as "much better" than the LFM forecast. Results of the 24 h step-mountain model forecast were subjectively judged to be similar to the NGM forecast and will not be shown here.

Case 1 may perhaps not look like a good candidate for tests of the present (dry) step-mountain model since it was chosen for NGM/LFM comparison primarily as being responsible for severe weather and a tornado outbreak with many deaths and injuries, followed by spring snowstorms across the Northeast. The initial time of this case was 0000 UTC 28 March 1984. At

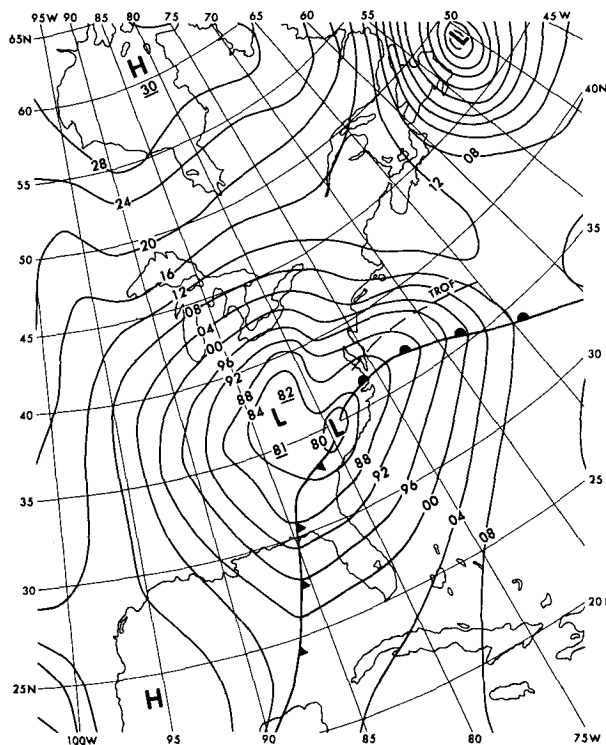


FIG. 12. Section of the U.S. National Weather Service surface analysis for 0000 UTC 29 March 1984.

that time a frontal wave was centered in Texas on a frontal line running farther east, roughly along the Gulf Coast. As the intensifying cyclone moved eastward, it developed a new center to the southeast of the original center. This double structure is seen on the NMC surface analysis for 0000 UTC 29 March, shown in Fig. 12. After 0300 UTC the original center (west of the Appalachians in the figure) disappears, while the eastern center deepens, setting some low barometric records and resulting in up to 75 cm of snow across interior sections of Pennsylvania, New York, and New England. NGM forecast for this case was ranked as "better" than LFM. However, neither the NGM forecast nor the LFM forecast showed the redevelopment in Georgia. Therefore, nine additional forecasts were made by Collins and Tracton to test the sensitivity of the forecast to various factors; one of them was a "silhouette terrain" forecast, differing from control by using the NGM version of silhouette mountains (Hoke et al. 1985). None of the nine sensitivity runs indicated the redevelopment. The same case was studied by Kocin et al. (1984). In spite of a 47 km grid distance and a 12 h later starting time for their integrations, their results do not show an obvious improvement over those of Hoke et al.

The 24 h step-mountain forecast for this case, with model parameters as described, was judged to be of about the same quality as that of various NGM runs. There was no indication of the redevelopment; the low, centered in the northwestern tip of Georgia, had inner

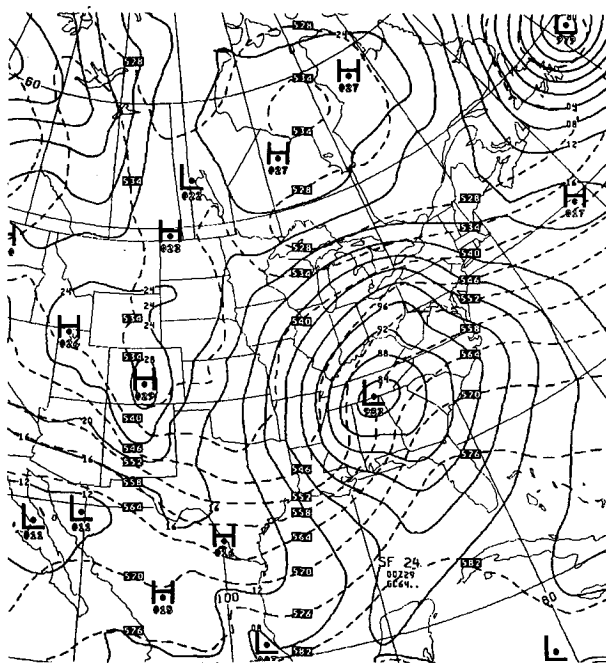


FIG. 13. Section of a 24 hour simulation of sea level pressure (solid lines) and 1000–500 mb thickness (dashed lines), using terrain derived from NMC "spectral" mountains, and verifying at 0000 UTC 29 March 1984.

isobars of a circular shape, with hardly any signs of ridging on its northeastern side.

A sensitivity experiment was performed with model parameters the same as those used for this forecast, except that the vertical resolution and distribution of model layers was changed to that of the 16-layer NGM structure. A section of the sea level pressure and 1000–500 mb thickness map obtained as a result of this experiment is shown in Fig. 13. In comparison with results of the nine-layer run, the ridging seen to the northeast of the center represents a clear hint of redevelopment, more so than can be seen in any of the nine NGM sensitivity experiments.

Since in view of the described mountain derivation procedure the change in vertical resolution has necessarily involved a change in model mountains—perhaps an increase in the height of Appalachians—the question has arisen as to whether the increased vertical resolution or the changed mountains were primarily responsible for the resulting ridging. Therefore, hoping to discriminate between these two possibilities, an experiment was performed in which the "spectral" mountains as input for the derivation of the step-mountain terrain were replaced by the mentioned NGM "silhouette" mountains. The result of this experiment is shown in Fig. 14. A very much increased intensity of the ridging can be seen, with a clear indication of the redevelopment over Georgia and South Carolina.

One may still wonder to what extent the success in the simulation of the (presumably) "trigger" stage of

redevelopment east of the Appalachian Mountains came as a result of the numerical technique employed and to what extent it is simply a result of higher mountains. In this connection it should be recalled that in mentioned experiments with the NGM model the use of higher mountains (Run 6, Fig. 11 in Collins and Tracton 1985) in no way gave a result that was superior to the general level of the remaining nine (including control) runs. Thus, a substantial difference in the ability of the two models to show sensitivity to the effect of higher mountains has apparently been identified, and this difference can only be explained as a result of the difference in numerical schemes of the two models.

## 7. Code efficiency

The two major problems concerning vectorization of the model are the internal horizontal boundaries inherent to the blocking techniques and the structure of the *E* grid.

The internal boundary problem is solved by defining masks, which are set to zero underneath the topography and to one otherwise. In this way, exactly the same arithmetic operations are performed at all grid points, regardless of whether they are in the atmosphere or under the ground. The same method is used to distinguish between land and sea.

As in the case of the internal boundaries, in order to provide different treatment along the lateral boundaries of the integration domain, the masks consisting of zeros and ones are used.

However, the problems arising due to the structure of the *E* grid were more difficult to cope with. Unlike

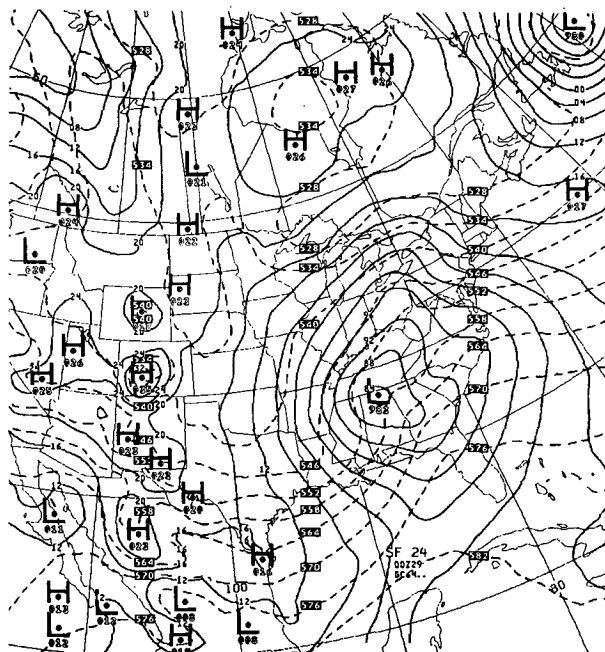


FIG. 14. As in Fig. 13 but using terrain derived from NMC "silhouette" mountains.

the other grids, if the horizontal indices are defined in the most straightforward manner, the indices of the grid points surrounding the grid point at which the calculation is performed cannot be calculated by simply adding or subtracting a constant increment. For the same pattern of grid points, the increment will depend on whether the indices of the reference point are even or odd. Thus, for efficient coding on vector machines, another method has to be looked for.

A possible solution for the hemispheric or global models was suggested by Janjić and Mesinger (1984). With this approach the column-wise horizontal index does not follow the constant longitude coordinate lines. Instead, as shown in Fig. 15, going from south to north the points in two consecutive rows with the same row-wise index are shifted with respect to each other for the longitudinal grid distance. This method was successfully used in a hemispheric model by Ničković (1982), but it would be impractical for use in a model intended for limited area integrations.

For this reason, a one-dimensional horizontal indexing was devised, schematically represented in Fig. 16. As indicated in the example shown in the figure, the one-dimensional index  $K$  increases row-wise from left to right and, reaching the right end of a row, jumps to the left end of the next row above. The velocity points denoted by the asterisks at the right ends of the rows, with odd two-dimensional latitudinal indices  $J$ , have the same one-dimensional indices  $K$  as the height points to the left of them, but are actually located at the left end of the next row above.

With this indexing, the horizontal indices of the grid points surrounding the point at which the calculation is performed are easily calculated adding constant increments. This makes coding straightforward, and the resulting code is easily readable. An additional advantage of the one-dimensional indexing is the large arrays processed in the innermost loops, which on some vector computers result in faster computations.

In order to ensure easy portability, the vector code

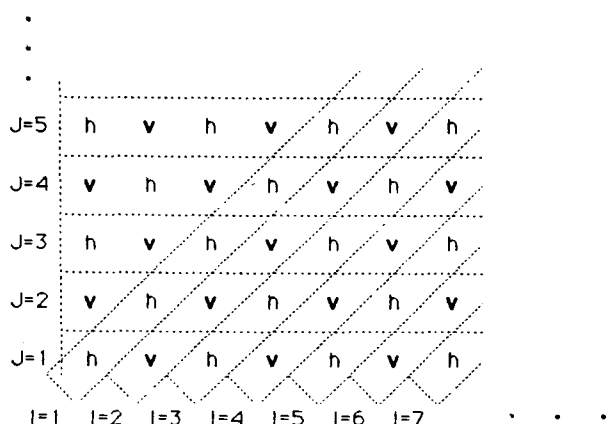


FIG. 15. Schematic representation of efficient two-dimensional indexing on the  $E$  grid suitable for a hemispheric/global model.

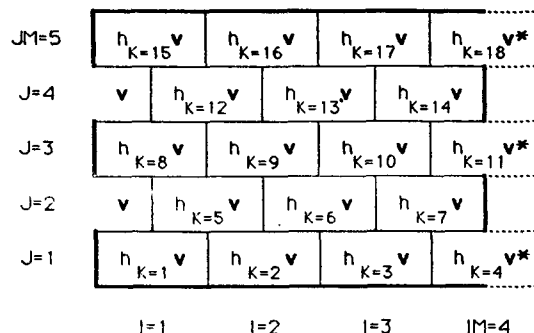


FIG. 16. Schematic representation of efficient one-dimensional indexing on the  $E$  grid suitable for both limited area and hemispheric/global area integrations. The values of the one-dimensional index  $K$  are displayed for each double grid-box containing both the velocity and height points. The velocity points denoted by the asterisk are physically located at the beginning of the next upper row, although they share the same index with the height point at the end of the preceding row.

was written following, to the maximum possible extent, the standard ANSI FORTRAN 77. The only deviation from the standard was the CYBER 205 half-precision extension using 32-bit word internal representation.

The vector code was more than ten times faster than the original scalar code, and with the CYBER 205 half-precision extension, this factor was further increased to over 15. A comparison with a carefully designed vector code used operationally shows that the efficiency standard required in an operational environment has been achieved, although no special vector machine extensions were used.

## 8. Conclusions

The effects of the errors inherent to the sigma system are for the first time demonstrated in real data runs. Namely, in two parallel integrations performed in the sigma and eta coordinate modes, with the same model code and model parameters, the sigma system runs showed increased noisiness, particularly in temperature fields at higher levels. One may speculate that this difficulty is related to the sigma system pressure gradient force error. Namely, the mass field may have been forced to adjust to the erroneous wind field produced by the false pressure gradient force. In any case, this remains a problem that requires further investigation.

In all numerical simulations performed, the eta coordinate model has shown considerable skill, in both relative and absolute terms. It has performed better than its sigma coordinate version in both parallel runs. The forecasts produced by the eta model have shown a high degree of realism and can be considered successful from the synoptic point of view. In a situation of particular interest, that of the redevelopment east of the Appalachian Mountains, it has shown the ability to forecast the onset stage of the phenomenon. This ability was lacking in another model of about the same horizontal and vertical resolution.

The price for these rewards is not excessive, if any at all. The governing equations in the eta coordinate are almost as simple as in the sigma system and, as our experience has shown, can be implemented in an existing sigma coordinate model without much effort. This is not surprising since the eta system can be considered as a generalization of the sigma coordinate; as already mentioned, the eta coordinate model can be run in the sigma mode simply by setting a switch in the code.

No problems have been encountered with the internal horizontal boundaries between the step-mountains and the free atmosphere. Moreover, it has been demonstrated that a physically well justified boundary condition can be formulated in such a way as to satisfy complex conservation constraints on nonlinear quantities. At the same time, this was the simplest possible no-slip boundary condition, that of setting the velocity components to zero at the boundaries and at the fictitious velocity points inside the mountains. Having in mind also the experience of Aragão of the University of Miami (personal communication), the internal boundaries can hardly be considered a problem any longer.

In contrast to what may appear at first glance, it has also been demonstrated that the eta coordinate model code can be, and has been, easily vectorized in the most straightforward manner.

A separate problem is the vectorization on the  $E$  grid. This problem has been resolved by one-dimensional horizontal indexing. In addition, as a by-product of the one-dimensional indexing, large matrices are processed in the innermost loops, which is a favorable feature on some vector machines.

In summary, we believe we have demonstrated that the eta coordinate is not only competitive, but also has visible advantages over the sigma coordinate, which, at present, is used almost exclusively. This should come as no surprise. The sigma system was devised 30 years ago, at a time when the available computer power allowed only very low horizontal and vertical resolution (typically about 400 km in the horizontal, and several layers in the vertical). As a result, only smooth, gently sloping terrain heights could be used. However, with increased resolution, allowing more realistic representation of topography, the well-known sigma system problems have become more apparent. As pointed out by several authors, they can be alleviated to a certain extent, but never eliminated completely. In such a situation, it seems natural to search for an alternative that will be better suited for currently used as well as future high-resolution models. We feel that, with its simplicity, performance, and easy implementation in the existing sigma coordinate models, the eta coordinate is a promising candidate.

*Acknowledgments.* The work reported here was made possible as a result of many factors. Foremost among these is a visit of the first of the authors (FM) to the

Geophysical Fluid Dynamics Program, Princeton University. In this connection, he is pleased to express his appreciation to Dr. Isidoro Orlanski, then Acting Director of the Geophysical Fluid Dynamics Laboratory and Head of the Mesoscale Dynamics Group, who hosted the program, as well as to Dr. Kikuro Miyakoda, Head of the Experimental Prediction Group, for warm hospitality, support, and encouragement. Just as much, he, and also Zaviša Janjić, are pleased to acknowledge the support and encouragement of Dr. William Bonner, Director, U.S. National Meteorological Center, who has enabled continuation of this work as part of the program of their visits to the Development Division of this Center. Thanks are due to the late Dr. John A. Brown, Jr., Head of the Division, for warm hospitality and support during their visits.

Dr. Jack J. Katzfey of the Mesoscale Dynamics Group of the Geophysical Fluid Dynamics Laboratory contributed substantially to the work reported by partly developing and enabling the use of a contouring package for our European region. Mr. Robert F. Strickler, while active, but also including the time after his retirement during the course of this work, spared no efforts in helping with file manipulations and successfully recovered pieces of data information essential for the completion of this study, even though they were clearly older than their typical survival age.

Many more people in various ways contributed to this work. In particular, a comment of Dr. Briant McAvaney led to the discovery of the indexing scheme shown in Fig. 16.

Numerous suggestions made by Dr. Bruce Ross of the Mesoscale Dynamics Group of the Geophysical Fluid Dynamics Laboratory have much improved the readability of the manuscript. Additional helpful suggestions were received from two anonymous reviewers.

The work was partly supported by the Association for Science of the S.R. of Serbia.

## APPENDIX

### Energy Conservation and the $\omega\alpha$ Term

Here the procedure will be outlined leading to an energy conserving scheme for the  $\omega\alpha$  term of the  $\eta$  coordinate thermodynamic equation. As we shall see, this procedure is analogous to that used in the  $\sigma$  coordinate system.

The zonal and meridional components of the pressure gradient force, denoted respectively by PGFU and PGFV, are defined at the  $v$  points, and at the model's layer  $k$  they have the form

$$\begin{aligned} \text{PGFU}_k = & -1/(2h_1 \Delta\lambda) \left\{ \frac{1}{3} [(\Delta_{\lambda'} \bar{\Phi}^{\eta'} + \Delta_{-\varphi'} \bar{\Phi}^{\eta'}) \right. \\ & + (RT/\bar{p}^{\eta'})_{\Delta_{\lambda'} \bar{p}^{\eta'}} + (RT/\bar{p}^{\eta'})_{\Delta_{-\varphi'} \bar{p}^{\eta'}}] \\ & + \frac{2}{3} (1/\Delta \bar{p}^{\lambda}) [(\Delta \bar{p}^{\lambda'} \Delta_{\lambda'} \bar{\Phi}^{\eta'} + \Delta \bar{p}^{\varphi'} \Delta_{-\varphi'} \bar{\Phi}^{\eta'}) \end{aligned}$$

$$\begin{aligned}
 & + \overline{\Delta \bar{p}^{\lambda'} (RT/\bar{p}^{\eta \lambda'})}_{\Delta_{\lambda} \bar{p}^{\eta \varphi'}} \\
 & + \overline{\Delta \bar{p}^{\varphi'} (RT/\bar{p}^{\eta \varphi'})}_{\Delta_{-\varphi'} \bar{p}^{\eta \lambda'}} \Big]_k, \\
 \text{PGFV}_k = & -1/(2h_2 \Delta \varphi) \Big\{ \frac{1}{3} [(\overline{\Delta_{\lambda'} \bar{\Phi}^{\eta \varphi'}} - \overline{\Delta_{-\varphi'} \bar{\Phi}^{\eta \lambda'}}) \\
 & + (\overline{(RT/\bar{p}^{\eta \lambda'})}_{\Delta_{\lambda} \bar{p}^{\eta \varphi'}} - \overline{(RT/\bar{p}^{\eta \varphi'})}_{\Delta_{-\varphi'} \bar{p}^{\eta \lambda'}}) \\
 & + \frac{2}{3} (1/\Delta \bar{p}^{\varphi}) [(\overline{\Delta \bar{p}^{\lambda'} \Delta_{\lambda'} \bar{\Phi}^{\eta \varphi'}} - \overline{\Delta \bar{p}^{\varphi'} \Delta_{-\varphi'} \bar{\Phi}^{\eta \lambda'}}) \\
 & + \overline{\Delta \bar{p}^{\lambda'} (RT/\bar{p}^{\eta \lambda'})}_{\Delta_{\lambda} \bar{p}^{\eta \varphi'}} \\
 & - \overline{\Delta \bar{p}^{\varphi'} (RT/\bar{p}^{\eta \varphi'})}_{\Delta_{-\varphi'} \bar{p}^{\eta \lambda'}}] \Big\}_k.
 \end{aligned}$$

Here,  $h_1$  and  $h_2$  are the metric coefficients defined by

$$h_1 = 1/(a \cos \varphi), \quad h_2 = 1/a,$$

where  $a$  is the radius of the Earth, and  $\lambda$  and  $\varphi$  are longitude and latitude, respectively. The distances between two neighboring mass and wind points in the directions of the coordinate axes  $\lambda$  and  $\varphi$  are denoted by  $\Delta\lambda$  and  $\Delta\varphi$ , respectively. The depths of the  $\eta$  layers in terms of pressure are denoted by  $\Delta\bar{p}$ . The axes  $\lambda'$  and  $\varphi'$  are defined by analogy with the "diagonal" coordinate axes  $x'$  and  $y'$  used in the plane geometry in the section dealing with the internal boundaries. The symbol  $\Delta$  followed by a subscript represents centered differences calculated along the axes indicated by the subscripts. The subscripts with negative signs indicate that the differences are calculated in the negative directions of the axes. Unless otherwise stated, as before, the overbars denote the simplest two-point averaging in the direction of the coordinate axis indicated by the accompanying superscript. The other symbols used have their usual meaning.

$$\begin{aligned}
 E_2 = \sum_T & -\frac{1}{3} (\Delta A/g)/(2h_1 h_2 \Delta \lambda \Delta \varphi) \{ u h_2 \Delta \varphi \Delta \bar{p}^{\lambda'} [(\overline{(RT/\bar{p}^{\eta \lambda'})}_{\Delta_{\lambda} \bar{p}^{\eta \varphi'}} + \overline{(RT/\bar{p}^{\eta \varphi'})}_{\Delta_{-\varphi'} \bar{p}^{\eta \lambda'}}) \\
 & + v h_1 \Delta \lambda \Delta \bar{p}^{\varphi} [(\overline{(RT/\bar{p}^{\eta \lambda'})}_{\Delta_{\lambda} \bar{p}^{\eta \varphi'}} - \overline{(RT/\bar{p}^{\eta \varphi'})}_{\Delta_{-\varphi'} \bar{p}^{\eta \lambda'}}) \Big\}_k. \quad (A3)
 \end{aligned}$$

The kinetic energy generation by the geopotential gradient part of the  $\frac{2}{3}$  term is given by

$$\begin{aligned}
 E_3 = \sum_v & -\frac{2}{3} (\Delta A/g) [u/(2h_1 \Delta \lambda) (\overline{\Delta \bar{p}^{\lambda'} \Delta_{\lambda'} \bar{\Phi}^{\eta \varphi'}} \\
 & + \overline{\Delta \bar{p}^{\varphi'} \Delta_{-\varphi'} \bar{\Phi}^{\eta \lambda'}}) + v/(2h_2 \Delta \varphi) (\overline{\Delta \bar{p}^{\lambda'} \Delta_{\lambda'} \bar{\Phi}^{\eta \varphi'}} \\
 & - \overline{\Delta \bar{p}^{\varphi'} \Delta_{-\varphi'} \bar{\Phi}^{\eta \lambda'}})]_k
 \end{aligned}$$

Dealing with the kinetic energy generation, it is convenient to split both the  $\frac{1}{3}$  and  $\frac{2}{3}$  terms into their geopotential and pressure gradient parts and then to consider separately the contribution of each of the four terms obtained in this way. Summing up the contribution of each of the geopotential gradient part of the  $\frac{1}{3}$  term over the  $v$  points, excluding the points inside the mountains, one obtains

$$\begin{aligned}
 E_1 = \sum_v & -\frac{1}{3} (\Delta A/g) \{ u \Delta \bar{p}^{\lambda'} / (2h_1 \Delta \lambda) [(\overline{\Delta_{\lambda'} \bar{\Phi}^{\eta \varphi'}} \\
 & + \overline{\Delta_{-\varphi'} \bar{\Phi}^{\eta \lambda'}})] + v \Delta \bar{p}^{\varphi} / (2h_2 \Delta \varphi) [(\overline{\Delta_{\lambda'} \bar{\Phi}^{\eta \varphi'}} - \overline{\Delta_{-\varphi'} \bar{\Phi}^{\eta \lambda'}})] \}_k, \quad (A1)
 \end{aligned}$$

where  $\Delta A = 4h_1 h_2 \Delta \lambda \Delta \varphi$  and  $g$  is gravity. As (A1) is to be used to determine an analog to  $\kappa T \omega / p$  ( $\omega \alpha$  term) carried at  $T$  points, the summation over the  $v$  points should be replaced by the summation over the  $T$  points in the free atmosphere. Assuming the cyclic boundary conditions, or a closed integration domain, after some algebra, (A1) can be rewritten in the form

$$\begin{aligned}
 E_1 = \sum_T & \frac{1}{3} (\Delta A/g) \bar{\Phi}_k^{\eta} / (2h_1 h_2 \Delta \lambda \Delta \varphi) [(\Delta_{\lambda} (u \Delta \bar{p}^{\lambda} h_2 \Delta \varphi) \\
 & + \Delta_{\varphi} (v \Delta \bar{p}^{\varphi} h_1 \Delta \lambda))]_k. \quad (A2)
 \end{aligned}$$

Here, the fluxes across the internal boundaries are set to zero in accordance with the boundary condition (4.1).

In a similar way, the pressure gradient part of the  $\frac{1}{3}$  term yields

$$\begin{aligned}
 E_2 = \sum_v & -\frac{1}{3} (\Delta A/g) \{ u \Delta \bar{p}^{\lambda'} / (2h_1 \Delta \lambda) [(\overline{(RT/\bar{p}^{\eta \lambda'})}_{\Delta_{\lambda} \bar{p}^{\eta \varphi'}} \\
 & + \overline{(RT/\bar{p}^{\eta \varphi'})}_{\Delta_{-\varphi'} \bar{p}^{\eta \lambda'}})] + v \Delta \bar{p}^{\varphi} / (2h_2 \Delta \varphi) \\
 & \times [(\overline{(RT/\bar{p}^{\eta \lambda'})}_{\Delta_{\lambda} \bar{p}^{\eta \varphi'}} - \overline{(RT/\bar{p}^{\eta \varphi'})}_{\Delta_{-\varphi'} \bar{p}^{\eta \lambda'}})] \}_k
 \end{aligned}$$

and, after rearrangement,

or, after rearrangement,

$$\begin{aligned}
 E_3 = \sum_v & -\frac{2}{3} (\Delta A/g) / (2h_1 h_2 \Delta \lambda \Delta \varphi) \\
 & \times [\overline{\Delta \bar{p}^{\lambda'} (u h_2 \Delta \varphi + v h_1 \Delta \lambda)}_{\Delta_{\lambda} \bar{\Phi}^{\eta \varphi'}} \\
 & + \overline{\Delta \bar{p}^{\varphi'} (v h_1 \Delta \lambda - u h_2 \Delta \varphi)}_{\Delta_{\varphi} \bar{\Phi}^{\eta \lambda'}}]_k. \quad (A4)
 \end{aligned}$$

Note that this time the summation is not performed over the  $T$  points; instead, the expressions under the summation sign are defined in between each pair of nearest  $T$  points. However, introducing the notation

$$u'd = \overline{uh_2\Delta\varphi + vh_1\Delta\lambda}^{\varphi'}, \quad v'd = \overline{vh_1\Delta\lambda - uh_2\Delta\varphi}^{\lambda'},$$

after some algebra, from (A4) one obtains

$$E_3 = \sum_T -\frac{2}{3} (\Delta A/g)/(2h_1 h_2 \Delta\lambda \Delta\varphi) \\ \times \{ \Delta_{\lambda'} (\overline{\Phi}^{\eta})^{\lambda'} \Delta \bar{p}^{\lambda'} u'd + \Delta_{\varphi'} (\overline{\Phi}^{\eta})^{\varphi'} \Delta \bar{p}^{\varphi'} v'd \\ - \overline{\Phi}^{\eta} [\Delta_{\lambda'} (\Delta \bar{p}^{\lambda'} u'd) + \Delta_{\varphi'} (\Delta \bar{p}^{\varphi'} v'd)] \}_k.$$

The first two terms in the curly brackets give zero contribution if the summation is performed over a closed domain, or a domain with cyclic boundary conditions. Thus,

$$E_3 = \sum_T \frac{2}{3} (\Delta A/g) \overline{\Phi}^{\eta} / (2h_1 h_2 \Delta\lambda \Delta\varphi) [\Delta_{\lambda'} (\Delta \bar{p}^{\lambda'} u'd) \\ + \Delta_{\varphi'} (\Delta \bar{p}^{\varphi'} v'd)]_k. \quad (A5)$$

The contribution to the kinetic energy generation of the remaining part of the  $2/3$  term is given by

$$E_4 = \sum_v -\frac{2}{3} (\Delta A/g) \{ u/(2h_1 \Delta\lambda) [\Delta \bar{p}^{\lambda'} (\overline{RT/\bar{p}}^{\eta})^{\lambda'}]_{\Delta_{\lambda'} \bar{p}^{\eta}}^{\varphi'} \\ + \Delta \bar{p}^{\varphi'} (\overline{RT/\bar{p}}^{\eta})^{\varphi'} \Delta_{-\varphi'} \bar{p}^{\eta} ] + v/(2h_2 \Delta\varphi) \\ \times [\Delta \bar{p}^{\lambda'} (\overline{RT/\bar{p}}^{\eta})^{\lambda'}]_{\Delta_{\lambda'} \bar{p}^{\eta}}^{\varphi'} - \Delta \bar{p}^{\varphi'} (\overline{RT/\bar{p}}^{\eta})^{\varphi'} \Delta_{-\varphi'} \bar{p}^{\eta} ] \}_k.$$

Similarly, replacing the summation over the  $v$  points by the summation over the  $T$  points, one finally obtains

$$E_4 = \sum_T -\frac{2}{3} (\Delta A/g)/(2h_1 h_2 \Delta\lambda \Delta\varphi) \\ \times \{ u'd \Delta \bar{p}^{\lambda'} (\overline{RT/\bar{p}}^{\eta})^{\lambda'} \Delta_{\lambda'} \bar{p}^{\eta} \\ + v'd \Delta \bar{p}^{\varphi'} (\overline{RT/\bar{p}}^{\eta})^{\varphi'} \Delta_{\varphi'} \bar{p}^{\eta} \}_k. \quad (A6)$$

Now we have reached the point at which the finite-difference approximation to the continuity equation has to be specified. Following Janjić (1984), we choose

$$\Delta W_k + \bar{\nabla} \cdot (\Delta p_k \mathbf{v}_k) = 0. \quad (A7)$$

Here the horizontal divergence operator has the form

$$\bar{\nabla} \cdot (\mathbf{v}_k \Delta p_k) = 1/(2h_1 h_2 \Delta\lambda \Delta\varphi) \\ \times \left\{ \frac{1}{3} [\Delta_{\lambda'} (uh_2 \Delta\varphi \Delta \bar{p}^{\lambda'}) + \Delta_{\varphi'} (vh_1 \Delta\lambda \Delta \bar{p}^{\varphi'})] \right. \\ \left. + \frac{2}{3} [\Delta_{\lambda'} (u'd \Delta \bar{p}^{\lambda'}) + \Delta_{\varphi'} (v'd \Delta \bar{p}^{\varphi'})] \right\}_k, \quad (A8)$$

and  $W$ , defined at the interfaces of the  $\eta$  layers, is the finite-difference analogue of  $\partial p/\partial t + \eta \partial p/\partial \eta$ .

Having defined the continuity equation approximation (A8), from (A2), (A5), and (A7),

$$E_1 + E_3 = \sum_T -(\Delta A/g) \overline{\Phi}^{\eta} \Delta W_k.$$

If we define the vertical averages of geopotential by

$$\overline{\Phi}_k^{\eta} = L_k \Phi_{k+1/2} + H_k \Phi_{k-1/2},$$

where the half-level values are carried at the interfaces of the  $\eta$  layers, and

$$L_k + H_k = 1,$$

after rearrangement

$$E_1 + E_3 = \sum_T -(\Delta A/g) [(\Phi_{k+1/2} W_{k+1/2} - \Phi_{k-1/2} \\ \times W_{k-1/2}) - \Delta \Phi_k (H_k W_{k+1/2} + L_k W_{k-1/2})]. \quad (A9)$$

After summation with respect to the vertical index, the contribution of the first term in the square brackets on the right-hand side of (A9) takes the form

$$\sum_{p_s} \Phi_s \partial p_s / \partial t.$$

Here the summation is performed over all pressure points at the ground surface. This term should remain uncompensated by the  $\omega\alpha$  term and, therefore, does not require further attention at this time.

Inspection of the remaining part of (A9) reveals that it represents an approximation to the integral with respect to mass of the expression  $-\alpha(\partial p/\partial t + \eta \partial p/\partial \eta)_k$ . Thus, the scheme

$$-(\Delta \Phi_k / c_p \Delta p_k) (H_k W_{k+1/2} + L_k W_{k-1/2}). \quad (A10)$$

which is a consistent approximation to  $(\alpha/c_p)(\partial p/\partial t + \eta \partial p/\partial \eta)_k$ , after being multiplied by  $c_p \Delta m = c_p \Delta p_k \times \Delta A/g$ , and summed up over the  $T$  points in the free atmosphere, will compensate exactly the considered part of  $E_1 + E_3$ .

Similarly, the sum of (A3) and (A6) represents an approximation to the integral with respect to mass of the expression  $-\alpha \mathbf{v}_k \cdot \nabla p_k$ . In the same way as in the case of (A10), one finds that the approximation to  $(\alpha/c_p) \mathbf{v}_k \cdot \nabla p_k$  of the form



$$\begin{aligned}
1/(c_p 2h_1 h_2 \Delta \lambda \Delta \varphi \Delta p_k) \Bigg\{ & \frac{1}{3} u h_2 \Delta \varphi \Delta \bar{p}^\lambda \left[ \overline{\overline{(RT/\bar{p}^\eta)^{\lambda'}} \Delta_{\lambda'} \bar{p}^\eta}^{\varphi'} + \overline{\overline{(RT/\bar{p}^\eta)^{\varphi'}} \Delta_{-\varphi'} \bar{p}^\eta}^{\lambda'} \right] \\
& + \frac{1}{3} v h_1 \Delta \lambda \Delta \bar{p}^\varphi \left[ \overline{\overline{(RT/\bar{p}^\eta)^{\lambda'}} \Delta_{\lambda'} \bar{p}^\eta}^{\varphi'} - \overline{\overline{(RT/\bar{p}^\eta)^{\varphi'}} \Delta_{-\varphi'} \bar{p}^\eta}^{\lambda'} \right] \\
& + \frac{2}{3} \left[ u' d \Delta \bar{p}^{\lambda'} \overline{\overline{(RT/\bar{p}^\eta)^{\lambda'}} \Delta_{\lambda'} \bar{p}^\eta}^{\varphi'} + v' d \Delta \bar{p}^{\varphi'} \overline{\overline{(RT/\bar{p}^\eta)^{\varphi'}} \Delta_{-\varphi'} \bar{p}^\eta}^{\lambda'} \right] \Bigg\}_k, \quad (A11)
\end{aligned}$$

after being multiplied by  $c_p \Delta m = c_p \Delta p_k \Delta A/g$  and summed up over the  $T$  points in the free atmosphere, will compensate exactly the contributions of  $E_2$  and  $E_4$ . Thus, (A10) and (A11) are the energy conserving scheme for the  $\omega\alpha$  term that we have been looking for.

In the pressure advection scheme in (A11), we recognize the four horizontal fluxes appearing in the Arakawa-type schemes. However, this scheme is not identical to the other schemes used in the model because of different averaging operators applied to define the values of  $(RT/p)$  in between the mass points.

#### REFERENCES

- Anthes, R. A., and Y.-H. Kuo, 1985: Error growth rates in limited-area models—summary of preliminary results. GARP Special Rep., No. 43, WMO, Geneva, III, 183–196. [Case Postale No. 5, CH-1211 Geneva 20, Switzerland.]
- Arakawa, A., 1970: Numerical simulation of large-scale atmospheric motions. *Numerical Solution of Field Problems in Continuum Physics*, Vol. 2, G. Birkhoff and S. Varga, Eds., SIAM-AMS Proc., Amer. Math. Soc., 24–40. [P.O. Box 6248, Providence, RI 02940.]
- , and V. R. Lamb, 1977: Computational design of the basic dynamical processes of the UCLA general circulation model. *Methods in Computational Physics*, Vol. 17, Academic Press, 173–265.
- , and —, 1981: A potential enstrophy and energy conserving scheme for the shallow water equations. *Mon. Wea. Rev.*, **109**, 18–36.
- Bates, J. R., and A. McDonald, 1982: Multiply-upstream, semi-Lagrangian advective schemes: Analysis and application to a multi-level primitive equation model. *Mon. Wea. Rev.*, **110**, 1831–1842.
- Bleck, R., 1977: Numerical simulation of lee cyclogenesis in the Gulf of Genoa. *Mon. Wea. Rev.*, **105**, 428–445.
- Buzzi, A., and S. Tibaldi, 1978: Cyclogenesis in the lee of the Alps: A case study. *Quart. J. Roy. Meteor. Soc.*, **104**, 271–287.
- Collins, W. G., and M. S. Tracton, 1985: Evaluation of NMC's regional analysis and forecast system—heavy precipitation events. *Preprints, Sixth Conf. on Hydrometeorology*, Indianapolis, Amer. Meteor. Soc., 289–296.
- Cullen, M. J. P., 1983: Current progress and prospects in numerical techniques for weather prediction models. *J. Comput. Phys.*, **50**, 1–37.
- , 1985: Developments in global modelling at the U.S. Meteorological Office. GARP Special Rep. No. 43, WMO, Geneva, I, 83–98. [Case Postale No. 5, CH-1211 Geneva 20, Switzerland.]
- Dell'Osso, L., 1984: High-resolution experiments with the ECMWF model: A case study. *Mon. Wea. Rev.*, **112**, 1853–1883.
- , and Dj. Radinovic, 1984: A case study of cyclone development in the lee of the Alps on 18 March 1982. *Contrib. Atmos. Phys.*, **57**, 369–379.
- Dragosavac, M., and Z. I. Janjić, 1987: Topographically induced stationary solutions of linearized shallow water equations on various grids. *Mon. Wea. Rev.*, **115**.
- Egger, J., 1972: Numerical experiments on the cyclogenesis in the Gulf of Genoa. *Beitr. Phys. Atmos.*, **45**, 320–346.
- Hoke, J. E., N. A. Phillips, G. J. DiMego and D. G. Deaven, 1985: NMC's regional analysis and forecast system—results from the first year of daily, real-time forecasting. *Preprints, Seventh Conf. on Numerical Weather Prediction*, Montreal, Amer. Meteor. Soc., 444–451.
- Janjić, Z. I., 1977: Pressure gradient force and advection scheme used for forecasting with steep and small scale topography. *Contrib. Atmos. Phys.*, **50**, 186–199.
- , 1979: Forward-backward scheme modified to prevent two-grid-interval noise and its application in sigma coordinate models. *Contrib. Atmos. Phys.*, **52**, 69–84.
- , 1984: Non-linear advection schemes and energy cascade on semi-staggered grids. *Mon. Wea. Rev.*, **112**, 1234–1245.
- , and F. Mesinger, 1984: Finite-difference methods for the shallow water equations on various horizontal grids. *Numerical Methods for Weather Prediction*, Seminar 1983, Vol. 1, ECMWF, Reading, U.K., 29–101. [Shinfield Park, Reading, Berkshire RG2 9AX, England.]
- Kasahara, A., 1974: Various vertical coordinate systems used for numerical weather prediction. *Mon. Wea. Rev.*, **102**, 509–522.
- Kocin, P. J., L. W. Uccellini, J. W. Zack and M. L. Kaplan, 1984: Recent examples of mesoscale numerical forecasts of severe weather events along the East Coast. NASA Tech. Memo. TM 86172, 57 pp. [NASA Accession No. N85-12523.]
- Kurihara, Y., 1968: Note on finite difference expressions for the hydrostatic relation and pressure gradient force. *Mon. Wea. Rev.*, **96**, 654–656.
- Mahrer, Y., 1984: An improved numerical approximation of the horizontal gradients in a terrain-following coordinate system. *Mon. Wea. Rev.*, **112**, 918–922.
- McDonnell, J. E., 1974: Notes on operational objective analysis procedure. [Internal manuscript, available from NOAA/National Meteorological Center, Washington, DC 20233.]
- Mesinger, F., 1971: Numerical integration of the primitive equations with a floating set of computation points: Experiments with a barotropic global model. *Mon. Wea. Rev.*, **99**, 15–29.
- , 1973: A method for construction of second-order accuracy difference schemes permitting no false two-grid-interval wave in the height field. *Tellus*, **25**, 444–458.
- , 1977: Forward-backward scheme, and its use in a limited area model. *Contrib. Atmos. Phys.*, **50**, 200–210.
- , 1981: Horizontal advection schemes of a staggered grid—an enstrophy and energy-conserving model. *Mon. Wea. Rev.*, **109**, 467–478.
- , 1982: On the convergence and error problems of the calculation of the pressure gradient force in sigma coordinate models. *Geophys. Astrophys. Fluid Dyn.*, **19**, 105–117.
- , 1984: A blocking technique for representation of mountains in atmospheric models. *Riv. Meteor. Aeronautica*, **44**, 195–202.
- , and Z. I. Janjić, 1985: Problems and numerical methods of the incorporation of mountains in atmospheric models. *Large-*

- Scale Computations in Fluid Mechanics*, Part 2: Lect. Appl. Math., Vol. 22, Amer. Math. Soc., 81–120. [P.O. Box 6248, Providence, RI 02940.]
- , and R. F. Strickler, 1982: Effects of mountains on Genoa cyclogenesis. *J. Meteor. Soc. Japan*, **60**, 326–338.
- Mihailović, D. T., and Z. I. Janjić, 1986: Comparison of methods for reducing the error of the pressure gradient force in sigma coordinate models. *Meteor. Atmos. Phys.*, **35**, 177–184.
- Miyakoda, K., 1973: Cumulative results of testing a meteorological-mathematical model. The description of the model. *Proc. Roy. Irish Acad.*, **73A**, 99–130.
- Nakamura, H., 1978: Dynamical effects of mountains on the general circulation of the atmosphere. I: Development of finite-difference schemes suitable for incorporating mountains. *J. Meteor. Soc. Japan*, **56**, 317–340.
- Ničković, S., 1982: Construction and testing of schemes for horizontal advection on a sphere, maintaining integral properties on the *E* grid. (In Serbo-Croatian). Sc.D. thesis, Dept. Meteor., University of Belgrade, 102 pp. [P.O. Box 550, YU-11001 Belgrade, Yugoslavia.]
- Phillips, N. A., 1957: A coordinate system having some special advantages for numerical forecasting. *J. Meteor.*, **14**, 184–185.
- Richards, P., and M. W. Stubbs, 1974: An intense April depression. *Weather*, **29**, 426–430.
- Rousseau, D., and H. L. Pham, 1971: Premiers résultats d'un modèle de prévision numérique à courte échéance sur l'Europe. *La Météorologie*, **20**, 1–12.
- Sadourny, R., 1985: Midlatitude systematic errors in numerical models. GARP Special Rep. No. 43, WMO, Geneva, III, 156–174. [Case Postale No. 5, CH-1211 Geneva 20, Switzerland.]
- Simmons, A. J., and D. M. Burridge, 1981: An energy and angular-momentum conserving vertical finite-difference scheme and hybrid vertical coordinates. *Mon. Wea. Rev.*, **109**, 758–766.
- Smagorinsky, J., J. L. Holloway, Jr. and G. D. Hembree, 1967: Prediction experiments with a general circulation model. *Proc. Inter. Symp. Dynamics Large Scale Atmospheric Processes*, Nauka, Moscow, U.S.S.R., 70–134.
- , S. Manabe and J. L. Holloway, Jr., 1965: Numerical results from a nine-level general circulation model of the atmosphere. *Mon. Wea. Rev.*, **93**, 727–768.
- Sundqvist, H., 1979: Vertical coordinates and related discretization. GARP Publ. Ser. No. 17, Vol. II, WMO, Geneva, 1–50. [Case Postale No. 5, CH-1211 Geneva 20, Switzerland.]
- Tibaldi, S., 1980: Cyclogenesis in the lee of orography and its numerical modelling, with special reference to the Alps. GARP Publ. Ser. No. 23, WMO, Geneva, 207–232. [Case Postale No. 5, CH-1211 Geneva 20, Switzerland.]
- , 1986: Envelope orography and maintenance of quasi-stationary waves in the ECMWF model. *Advances in Geophysics*, **29**, 339–374.
- Tomine, K., and S. Abe, 1982: A trial to reduce truncation errors of the pressure gradient force in the sigma coordinate systems. *J. Meteor. Soc. Japan*, **60**, 709–716.
- Undén, P., 1980: Changing the spherical grid for LAMs. Limited area modeling. *LAM Newsletter*, **1**, No. 1, 12–16. [SMHI, Box 923, Norrköping, Sweden.]
- Vasiljević, D., 1982: The effect of Mesinger's procedure for preventing grid separation on the geostrophic mode. *Contrib. Atmos. Phys.*, **55**, 177–181.
- Wallace, J. M., S. Tibaldi and A. J. Simmons, 1983: Reduction of systematic forecast errors in the ECMWF model through the introduction of an envelope orography. *Quart. J. Roy. Meteor. Soc.*, **109**, 683–717.
- Winninghoff, F. J., 1968: On the adjustment toward a geostrophic balance in a simple primitive equation model with application to the problems of initialization and objective analysis. Ph.D. thesis, Dept. of Meteorology, University of California, Los Angeles.
- WMO-ICSU, 1974: *Modelling for the First GARP Global Experiment*. GARP Publ. Ser. No. 14, WMO, Geneva, 262 pp. [Case Postale No. 5, CH-1211 Geneva 20, Switzerland.]